East Asian monsoon and westerly jet driven changes in climate and surface conditions in the NE drylands of China since the Late Pleistocene

Steve Pratte, Kushan Bao, Chuxian Li, Wenfang Zhang, Gaël Le Roux, Gaojun Li, François de Vleeschouwer

East Asian monsoon and Westerly Jet driven changes in climate and surface conditions in the NE drylands of China since the Late Pleistocene

Steve Pratte[1,3], Kushan Bao[2,3], Chuxian Li[4], Wenfang Zhang[3], Gaël Le Roux[5], Gaojun Li[6], and François De Vleeschouwer[7]

[1] School of Earth Sciences, Zhejiang University, Hangzhou, China

[2] School of Geography, South China Normal University, Guangzhou 510631, China

[3] State Key Laboratory of Lake Science and Environment, Nanjing Institute of Geography and Limnology, Chinese Academy of Sciences, Nanjing, China

[4] Institute of Geography and Oeschger Center for Climate Change Research, University of Bern, 3012 Bern, Switzerland

[5] Laboratoire écologie fonctionnelle et environnement, Université de Toulouse, CNRS, INPT, UPS, Toulouse, France

[6] Key Laboratory of Surficial Geochemistry, Department of Earth and Planetary Sciences, Nanjing University, Nanjing, China

[7] Instituto Franco-Argentino para el Estudio del Clima y sus Impactos (UMI IFAECI/CNRS-CONICET-UBA-IRD), University of Buenos Aires, Buenos Aires, Argentina

Corresponding author: Kunshan Bao (ksbao@scnu.edu.cn)

Abstract

The East Asian summer monsoon (EASM) is a major component of the global climate yet, the causes for the past spatiotemporal variability of EASM rainfall, its interactions and impacts remain unresolved. Here we use the Sr-Nd isotopes and rare earth elements composition of dust in a peat record from northeast (NE) China to investigate the relationship between the East Asian monsoon and Westerly Jet (WJ) over East Asia since the Late Pleistocene (14 cal ka BP). The NE drylands of China dominate the dust fraction (Hunshandake, Horqin; 44-88%) with a contribution from the deserts of NW China (Badain Jaran, Tengger, Taklamakan; 10-44%), suggesting an influence of the WJ. Dust deposition varied during the Holocene, displaying a minimum between 8.0-6.0 cal ka BP and two peaks at 5.8-3.8 and 1.7-0.3 cal ka BP. Changes in dust flux are opposite to the East Asian winter monsoon intensity profile, suggesting a limited influence of the winter monsoon. The EASM appears to have played a more significant role in the dust cycle, with increasing dust fluxes corresponding with lower EASM precipitation. Variations in dust flux from NE drylands display shifts reflecting changes in EASM precipitations and dune activity along the EASM margin, where the dust originates from. To account for the influence of the WJ, we propose that the meridional position and intensity of the WJ also affected dust emission in the drylands' region. A more northward position of the WJ allows the EASM front further north, generating more precipitations over the NE drylands, reducing the extent of arid areas, and resulting in less dust emission from dune activity, while the opposite occurs with a strong, more southerly WJ. Anthropogenic activities are likely to have had an increasing impact on the dust cycle over the late Holocene. Nevertheless, the presence of inconsistencies in records, coupled with a simultaneous decline in climatic conditions (mainly precipitations) during the same timeframe, hinders the precise assessment of the influence of human activities on dust emissions in the region.

1. Introduction

The East Asian summer monsoon (EASM) has a major influence on global climate (An, 2000), controlling most aspects of hydrology in East Asia. Its extent, intensity, and associated precipitations display clear variations during the Holocene (Chen et al., 2015; Goldsmith et al., 2017) and have a considerable influence on the economy and lives of billions of people. Understanding its past variability, interactions, and impacts is important to determine its future response to climate change. The spatiotemporal heterogeneity in the Holocene maximum in monsoonal rainfall in northern China has long been a matter of debate, which prevents a complete understanding of the EASM behaviour and dynamics (An, 2000; Chen et al., 2015; Herzschuh et al., 2019; Li et al., 2020a; Zhou et al., 2016). Recently, evidence has pointed to interactions between the EASM and the northward position and orientation of the Westerly Jet (WJ) stream as an explanation for the spatiotemporal variations in EASM precipitations (Chiang et al., 2015; Herzschuh et al., 2019; Li et al., 2020b), and also for changes in the East Asian winter Monsoon (EAWM) (Nagashima et al., 2007). The position of the WJ has varied during the Holocene and has been found to affect EASM precipitations and temperature, conditions often being drier and colder in northern China when the WJ was further south and the opposite when it was in a northward position (Bae et al., 2020; Nagashima et al., 2013; Wang et al., 2020). Hence,

reconstructing paleo-synoptic conditions remains critical in the understanding of East Asian climate dynamics and its impacts on Earth's surface processes.

Mineral dust acts both as a driver and a recorder of climate changes, its emission, transport, and deposition being a function of a series of climatic and environmental factors, such as aridity, air mass trajectories, and human activities (Marx et al., 2018). Paleo-dust records produce clear evidence of the variability of dust deposition in response to climate changes and provide multi-proxy data on changes in aridity, synoptic systems, and wind strength (Kohfeld and Harrison, 2001; Marx et al., 2018; Nagashima et al., 2007) as well as anthropogenic activities. East Asia contains some of the world's largest dust sources, accounting for about a quarter of global dust emissions (Ginoux et al., 2004). The East Asian monsoon (EAM) and WJ affect East Asian climate variability, induce changes in surface conditions in source regions and have considerable effects on dust emission (Sun et al., 2001). Changes in dust levels also have important societal and environmental impacts (Goudie, 2009), e.g., Asian dust affects the biogeochemical cycle of P and Fe in the North Pacific (Letelier et al., 2019). Therefore, paleo-dust records downwind of source regions are important to better constrain the variability of the East Asian climate, but also the impacts of synoptic systems on atmospheric dust loadings.

Rare earth elements (REE) display very similar chemical properties and inherit their chemical composition from their source material. It is generally accepted that REE are not significantly affected by crustal weathering (McLennan, 1989; Nesbitt, 1979) and hence both their elemental and isotopic (Nd often combined with Sr or Pb) composition have been used to trace sediment provenance (Biscaye et al., 1997; Chen et al., 2007a; Ferrat et al., 2011; Gaiero et al., 2004; Gallet et al., 1998; McLennan, 1989). In East Asia, these paleo-provenance proxies have been used to characterize the deserts and dune fields of northern China (Chen et al., 2007a; Ferrat et al., 2011; Hu and Yang, 2016; Jiang and Yang, 2019; Nakano et al., 2004; Rao et al., 2008; Rao et al., 2011; Xie and Chi, 2016; Xie et al., 2020; Yang et al., 2009). The seminal work by Chen et al. (2007a) has shown that based on Sr-Nd isotopic compositions of specific size fractions (<75μm and <5 μm), the drylands of East Asia can be divided into three distinct regions owing to the source material from which they are derived (Fig. 1). These characteristic units have since been used extensively to trace the specific sources of dust in environmental archives and to reconstruct their related changes in the synoptic systems in Asia (Beaudon et al., 2022; Chen and Li, 2013; Ferrat et al., 2012; Miyazaki et al., 2016; Xie et al., 2019; Zhang et al., 2018a; Zhao et al., 2015).

Northeastern (NE) China, located downwind of the major dust sources of East Asia, is under the influence of both the EAM system and the WJ (Fig. 1). While dust records in peat from NE China show that dust is coming from the Chinese drylands (Fig. 1) (Pratte et al., 2020), the exact drylands are yet to be determined. In this study, we aim to utilize geochemical and isotopic signatures of the mineral fraction (i.e. dust component) in peat to constrain the dust source(s) to Hani peatland in NE China and identify associated climatic drivers (Fig. 1). In achieving this, we investigate the REE compositions and Sr-Nd isotopic signatures of peat in comparison to those of potential east Asian sources in the literature and from local sources collected near the study site. We further identify how the dominant atmospheric systems in East Asia (i.e. WJ and EAM) affected environmental changes in the dust source regions since the Late Pleistocene.

2. Materials and Methods

2.1 Study area and core collection

The Hani peatland (42°13'27.0''N; 126°31'110.0''E; 900 m.a.s.l.; 18 km^2) is located in the Jilin Province, NE China (Fig. 1A). The area is dominated by Quaternary volcanic deposits (alkali basalts, tholeiitic basalts, trachyte and pyroclastic deposits) forming the Longgang volcanic field (LGVF), which overlays the Upper Archean Anshan migmatite group, part of the North China craton and composed of migmatite, gneiss, amphibolite and quartzite (*Bureau of Geology and Mineral Ressources of Jilin Province, 1988*). The climate in the study area is governed by the East Asian monsoon and is characterized by a strong seasonality, with warm/moist conditions through the influence of air masses from the Pacific during the summer and cold/dry air masses from the Asian continent during winter (Schettler et al., 2006a). The EAWM and westerly winds strongly affect the region during winter and especially spring, when conditions are favourable for the occurrence of dust storms in spring (Chu et al., 2009). The study site is located in a region that was devoid of significant human activities that would have influenced local dust emission prior to the 18^{th} century (Makohonienko et al., 2008). As such, Hani peatland is an ideal record to study regional to large-scale dust transport.

Peat core collection, processing for physical characteristics and chronological control are detailed in Pratte et al. (2020). Briefly, a 10m profile, of which 9.3m is composed of peat (Hani-3), was collected from the Hani peatland. The core, dated by ^{14}C AMS (15 dates), shows that peat accumulation initiated around 14.5 cal ka BP (Fig. 1C). The representativity of the Hani peat record as a geochemical archive of aeolian dust as already been established (Pratte et al., 2020). Surface samples from potential local sources (soils, scoria, rocks) were collected near the study site to characterize the isotopic composition of local dust sources (Fig. 1B). The surface soils were separated as bulk and <63µm fractions, dried and ground while consolidated samples, e.g. basalt and scoria, were cut, ground and analyzed as bulk materials.

2.2 Sr-Nd isotopes analyses

Details on peat sub-sampling and sample preparation are described in Pratte et al. (2020). Homogenized and ashed (550°C for 6h) peat samples were processed and digested in an acid mixture (HNO_3-HF) following an established protocol (Zhang et al., 2016). The siliciclastic Sr-Nd isotopic ratios of 46 peat samples, one scoria, one rock and three soil samples (bulk and <63µm) were determined by multi-collector ICP-MS at Nanjing University after elution through a series of anionic resins. Replicate analyses of the SRM987 ($^{87}Sr/^{86}Sr$ = 0.71034±0.00026) and JMCNd_2O_3 (Nd oxide) certified reference materials (CRM) yielded values of 0.710268±13 (n=9) and 0.512093±7 (n=7) respectively. The chemical procedure was verified using the BCR-2 CRM ($^{87}Sr/^{86}Sr$ = 0.705000±11; $^{143}Nd/^{144}Nd$ = 0.512637±13) showing values of 0.705029±0.9 (n=2) and 0.512627±6 (n=2) for $^{87}Sr/^{86}Sr$ and $^{143}Nd/^{144}Nd$ respectively. The Nd isotopic composition of 29 additional samples was determined by TIMS at *Observatoire Midi-Pyrénées* in Toulouse following

Vanneste et al. (2015). Instrumental drift was monitored using Nd reference material La Jolla ($^{143}Nd/^{144}Nd$ = 0.511858) for which values of 0.511843±11 (n=11) were obtained. Procedural blanks for Nd are negligible, while replicate samples between the two measurement methods were generally within the $^{143}Nd/^{144}Nd$ values error bars. The $^{87}Sr/^{86}Sr$ of the Hani samples was corrected for the proportion of <2µm particles (see section 2.4). Rare earth element and Sr concentrations were previously measured (Pratte et al., 2020) on dry powdered peat (~100 mg) using Q-ICP-MS and are used as a support for Sr-Nd data and to reconstruct the dust flux (see Fig. 2, Table S1). The most probable sources for the dust were identified and used as end members (Fig. S2) to estimate their respective contributions based on the hyperbolic mixing relationship of ratio-ratio plots (section 2.3).

Epsilon neodymium (εNd) was calculated according to DePaolo and Wasserburg (1976):

(1) $$\varepsilon\mathrm{Nd} = \left(\frac{\left(\frac{143\mathrm{Nd}}{144\mathrm{Nd}}\right)}{0.512638} - 1\right) \times 10000$$

where 0.512638 corresponds to the chondritic uniform reservoir (CHUR) and represents present-day average Earth value (Jacobsen and Wasserburg, 1980).

2.3 End member calculation and source related dust flux

Comparing the Sr-Nd isotopic composition and REE ratios of the Hani peat samples with those of the potential source areas in northern China (Fig. 1A), the most probable sources for the mineral dust were identified and used as end members (median values; Fig. S2) to estimate their respective contribution. The contribution of each source end-member was calculated based on the hyperbolic mixing relationship of ratio-ratio plots as described in Albarède (1995):

(2) $$\left(\frac{C^{i2}}{C^{i1}}\right)_{mix} = \frac{\sum_{j=1}^{n} C_j^{i2} f_j}{C_{mix}^{i1}}$$

Where C^{i1} and C^{i2} are the Nd and Sr isotopes or REE concentrations in a mixture of *n* end-members *j*, while *f* represents the fraction of end-member *j* in the mineral fraction recovered in samples of Hani peatland. The most probable source proportions were determined using the root mean square error (RMSE), where a value close to zero correspond to a closer fit to the measured value (Table S3). This approach was successfully applied to trace the source of aeolian dust deposited to a peatland from Amsterdam Island in the Indian Ocean (Li et al., 2020).

The dust accumulation rate, i.e. dust flux (g m^{-2} a^{-1}) was calculated using the sum of REE following the formula:

(3) $$Dust\ flux_i = \frac{\sum[REE]_i \times PAR_i \times \sigma_i}{\sum[REE]_{UCC}} \times 10000$$

where $\sum[REE]_i$ is the sum of REE concentrations in a specific sample i, $\sum[REE]_{UCC}$ is the sum of REE concentrations in the upper continental crust (143 µg g^{-1}; (Wedepohl, 1995)), PAR is the peat accumulation rate (cm a^{-1}) calculated based on the age-depth model and σ is the bulk density of

the sample (g cm^{-3}). Afterward, the relative proportion of dust contribution from specific sources (Fig. 5 and S3) were used to estimate their specific dust deposition flux (ex.: dust flux from NE drylands in Fig. 6 and 7).

The resulting source-specific dust fluxes were submitted to change point analysis to identify significant shifts in the dust record. The change point analysis was performed using the Change-point Analyzer 2.0 software (Taylor Enterprise). The method combines cumulative sum charts (difference between the values and the average) and bootstrapping to detect changes (Taylor, 2000). Ten thousand bootstraps were performed and only changes with probabilities greater than 99% were considered.

2.4 $^{87}Sr/^{86}Sr$ as a dust proxy in peat and potential grain size effect on $^{87}Sr/^{86}Sr$ values

Sr is known to be affected by mineral dissolution and diffusion in peat (Shotyk, 1997; Steinmann and Shotyk, 1997), which can affect its reliability as a proxy of dust deposition and provenance. Sr concentrations in Hani-3 profile are generally low with an average of 21±6 μg g^{-1} above 635 cm of depth (excluding the peak around 180 cm) for 41±12 μg g^{-1} below (Fig. 2), a difference much lower than those observed in records affected by Sr remobilization (Pratte et al., 2017; Steinmann and Shotyk, 1997). This suggests that mineral dissolution and Sr remobilization is limited in the Hani-3 core and that it can be used as a dust archive. Furthermore, after removing the potentially labile fraction of Sr through a weak acid treatment, the trends in the $^{87}Sr/^{86}Sr$ signal closely follow those of the εNd (Fig. 2), which confirms that the labile fraction was removed and that the $^{87}Sr/^{86}Sr$ represents the siliciclastic fraction and can be used to reconstruct changes in dust source(s).

The grain size of the Hani samples is generally dominated by silts with a median grain size of 10-18.7 μm and more than 95% in the <75 μm fraction (Fig. S1; (Pratte et al., 2020)), which makes them comparable with the potential sources in the literature. The loess deposits of NE China display lower $^{87}Sr/^{86}Sr$ values than most Hani samples, but very similar εNd (Fig. 3). The influence of grain size sorting on Sr isotopic ratios is well documented, with higher ratios being reported in finer fractions (<2μm and <5 μm) (Biscaye et al., 1997; Chen et al., 2007a; Feng et al., 2009; Grousset et al., 1992; Meyer et al., 2011). This is supported by the fact that the loess grain size is generally coarser than that of the Hani samples. This can likely be explained by the Hani peatland location, i.e. at further distances from the NE drylands than the loess deposit and in a mountain range, the Changbai Mountains, that likely partially intercept coarser particles. Given the low amounts of samples available, it was not possible to separate the <2 μm fraction of the mineral matter in Hani and analyse it separately for $^{87}Sr/^{86}Sr$. Instead we elected to make a correction to the $^{87}Sr/^{86}Sr$ values of the bulk samples based on the proportion of <2 μm particle in each sample analysed (Fig. S3). The clay particles (<2 μm) of the Chinese drylands have $^{87}Sr/^{86}Sr$ ratios 0.006 higher on average than the other grain size fraction (Chen et al., 2007a). The <2 μm fraction in Hani samples range between 6 and 17%, which corresponds to an estimated maximum increase of 0.001 in the $^{87}Sr/^{86}Sr$ ratios of the Hani samples.

3. Results

3.1 Summary of the core general characteristics

A detailed description of the physical characteristics of the core is given in Pratte et al. (2020) and a summary of the key data is presented in Fig. 2. The peat is generally dominated by sedges with *Sphagnum* spp. present in various proportions down to 931 cm of depth. Lithological changes in the peat core correspond mainly to variations in decomposition state and color along with the presence of noticeable mineral-rich layers at 1.7-1.8, 10.6-10.7, 11.2-11.4 and 11.9-12.0 cal ka BP (Fig. S1). The ash content of the peat ranges between 5-58% with an average of 21±4% during the Holocene, when excluding the mineral-rich layers, which is lower and more stable than the older part (>11.5 cal ka BP) of the core (30±8%). The particle grain size of the mineral fraction of peat is usually dominated by a mode in the fine-silt fraction, but still displays a similar pattern as ash content, i.e. samples with greater median grain size are more frequent in the lower part of the core and in the mineral-rich layers.

3.2 Geochemical composition of the peat

Isotopic compositions of $^{87}Sr/^{86}Sr$ and εNd samples from Hani and local sources are shown in Fig. 3 and Table S2. The εNd of the peat samples ranges between -0.5 and -9.8, while the $^{87}Sr/^{86}Sr$ varies from 0.704687 to 0.715998 (Fig. 3 and Table S3). The εNd of the scoria and rocks is +1.1 and +1.7, while $^{87}Sr/^{86}Sr$ values are 0.704555 and 0.704418 (Fig. 3). The isotopic composition of the soils ranges between that of the scoria and volcanic rocks and of the Hani peat samples with values of +0.7 to -4.8 and 0.704618 to 0.707578 for εNd and $^{87}Sr/^{86}Sr$ respectively (Fig. 3).

REE patterns of the Hani peat samples, local sources (soils, scoria, volcanic deposits), and the <5 µm and <75 µm fractions from potential Chinese dust sources (deserts and dune fields; Fig. 1) are shown in Fig. 4A-B. The greater part of the Hani samples displays relatively flat REE patterns with a slight enrichment in middle REE (Fig. 4B). These samples are also characterized by near-neutral Eu anomalies (Eu/Eu^*_N= 0.94-1.07). In comparison, a number of peat samples (n=19) also have a relatively flat REE pattern, but display a clear positive Eu anomaly (Eu/Eu^*_N>1.10) while three samples show lower light REE contents (Fig. 4C, red curves). Soils, scoria, and rock samples measured in this study and from the literature also display positive Eu/Eu^*_N anomalies ranging between 1.20 and 1.98 (Fig. 4C).

4. Discussion

4.1 Dust provenance

The comparison of the REE patterns of the Hani samples with those of potential sources confirms the mainly allochthonous origin of the dust (Pratte et al., 2020). Most of the Hani samples show a close resemblance to the patterns of the drylands and loess of northern China with a slight middle REE enrichment (Fig. 4A and B). However, the similarity of the REE patterns of the various

deserts and dune fields does not allow for the identification of the precise source on this basis. The presence of a positive Eu/Eu* anomaly in a number of samples (n=19) shows that local sources contribute significantly during specific events (Fig. 4C). In addition, samples with higher Eu/Eu* anomalies, especially those around 1.7 cal ka BP, generally contain more plagioclase feldspars (Pratte et al., 2020), known to display positive Eu anomalies (Wilson, 2000). Hence, the REE composition of the Hani sample allow the distinction between the local mafic source(s) from the allochthonous source(s) from the deserts and drylands of China.

As Chinese drylands were identified as the main source of mineral material in Hani peatland (Pratte et al., 2020), we use Sr-Nd isotopes, in conjunction with potential source areas, to narrow down the most likely drylands. These drylands are divided into three isotopic regions (Fig. 1a): 1) the drylands along the northern boundary of China (NBC: Hunshandake, Horqin, Hulun Buir, Songnen and Gurbantunggut); 2) the deserts along the northern margin of the Tibetan Plateau (NMTP: Taklamakan, Qaidam, Badain Jaran and Tengger), and 3) the deserts on or near the Ordos Plateau (Hobq and Mu Us) (Chen et al., 2007a). Most peat samples are within the fields of the NE drylands (NED; Hunshandake, Horqin, and Songnen) and the NMTP (Fig. 3). The εNd of the peat samples ranges between -0.5 and -9.8, while the $^{87}Sr/^{86}Sr$ varies from 0.704687 to 0.715998 (Fig. 3 and Table S3).

The εNd of local sources (1.7 for rock and 1.1 for scoria; average of 1.5) is higher than the Chinese drylands (average of -8.9 and -10.7 for NED and NMTP deserts respectively), while the $^{87}Sr/^{86}Sr$ is lower (0.704418 (rock) and 0.704555 (scoria) for an average of 0.704544 vs. 0.711065 (NED) and 0.723295 (NMTP)) (Fig. 3, S2 and S3, Tables S2). The deserts of the Ordos Plateau as well as the Badain Jaran and Tengger (isotopically part of the NMTP) have been invoked as a potential source of dust in the region (Zaarur et al., 2020). While the Ordos Plateau cannot be completely excluded as a minor source, the isotopic composition of the Hani samples is closer to the Badain Jaran and Tengger, which are geographically near the Ordos Plateau. A number of samples in the Hani record, mainly around 1.7, 10.7 and 13.0 cal ka BP, show a clear local signature (Fig. 2, 3, 5). Samples centered around 1.7 and 10.7 cal ka BP correspond in timing with volcanic eruptions from the Jinlongdingzi volcano, located ~14km NW, and recorded in several records in the region (Liu et al., 2009; Zhao et al., 2017). No eruptions have been reported around 13.0 cal ka BP, but tephra layers dated around 11.4 and 14.0 cal ka BP and geochemically linked to the Longgang volcanic field suggest there were some active volcanoes during that period (Liu et al., 2009). Another potential explanation for the lower $^{87}Sr/^{86}Sr$ and higher Eu anomalies and grain size around 13.0 cal ka BP, are flooding event or increased runoff from the surroundings of the peatland. Hani peatland was not as developed at that time and the coring location was closer to the edge of the peatland (Zhang et al., 2019), potentially resulting in a greater influx of local material at least sporadically. While the presence of volcanic glasses in the corresponding layers could not be confirmed given the limited amount of sample available, the clearly distinct signal in these layers and correspondence with local volcanic sources suggest Nd and Sr isotopes can help pinpoint volcanic eruptions (Le Roux et al., 2012) without having to find glass shards. Hence, they can be used as complementary tools to classical tephrastratigraphy.

The NE drylands dominate as a source since the Late Pleistocene (Fig. 3 and 5). The contribution of dust from the different sources was relatively stable except around 1.7 cal ka BP (local sources: >58%) and between 1.8-4.0 cal ka BP (NMTP sources: 41%) (Fig. 3 and 5). This dominance of dust from the NED is supported by modern dust observations. Modeling of dust emission in northern China between 2001-2014 shows that Inner Mongolia is a significant source (Du et al., 2018). Between 2000-2002, meteorological data shows that 8-30% of dust storm events originated in eastern Inner Mongolia (Hunshandake, Horqin) (Zhang and Gao, 2007). Isotopic and elemental geochemistry on Quaternary loess deposits in NE China (Xie et al., 2019; Zeng et al., 2020) points to the Hunshandake and Horqin deserts (Fig. 1) as the main sources of the dust in the region. While a large part of the samples displays a similar composition, some show slightly higher $^{87}Sr/^{86}Sr$ than the loess. This can likely be explained by the Hani peatland location, i.e. at further distances from the NED than the loess deposits and in a mountain range, the Changbai Mountains, that likely partially intercept a portion of dust from those drylands. This difference in location likely results in Hani peatland being more sensitive to contributions in dust from the NMTP. Excluding the peak potentially related to volcanic eruptions, the proportion of dust from the NED was greater prior to 10.0 cal ka BP.

Sr-Nd isotopes of the siliciclastic material from lake Sihailongwan (Zaarur et al., 2020), located to the northeast of Hani peatland, display a slightly different composition with higher εNd and lower $^{87}Sr/^{86}Sr$ (Fig. 3). Lake Sihailongwan is a maar lake developed in a volcanic crater, more likely to receive more local material from the carter rims, which could explain the different Sr-Nd composition between the two sites. This is supported by the higher Eu/Eu anomalies of the clastic material of lake Sihailongwan (Eu/Eu*PAAS = 1.15) in comparison to Hani (Eu/Eu*PAAS = 1.05) suggesting a greater proportion of volcanic material in the former. Such a difference in the proportion of locally derived material would be enough to explain the difference in Sr-Nd isotope composition between the two records. Other regional records, including lake Tuofengling, lake Tianchi and Motianling peatland further north and northwest of Hani peatland (Fiałkiewicz-Kozieł et al., 2022; Zhang et al., 2017; Zhou et al., 2023). Lake Tuofengling and Tianchi display composition closer to the Mongolian Plateau, which Zhang et al. (2023) explains by the more northern location of the two sites reducing the influence of the Westerlies on dust supply at those sites. Motianling peatland Sr-Nd composition is also similar to that of the Mongolian Plateau and the Hulun Buir sandy land which can be explained by its closer proximity to the two sources (Fiałkiewicz-Kozieł et al., 2022). In summary, the Sr-Nd isotope and REE composition suggest that the NE drylands of China, likely the Hunshandake and Horqin, are the main source of dust in Hani peatland.

4.2 Influence of the East Asian monsoon on the dust inputs

Dust flux values in the Hani record are high during the Late Pleistocene and gradually decrease starting at the early Holocene, a minimum is observed between 8.0-6.0 cal ka BP, followed by two peaks at 5.8-3.8 and 1.7-0.3 cal ka BP (Fig. 6D and 7K). Changepoint analysis on the dust flux from NED identified four changes (>99% confidence level) in the record at 1.8, 3.8, 5.7 and 11.9 cal ka BP. Some slight differences are present between the REE-based dust flux (Fig. D; white and

grey curve) and the NED dust flux (Fig. 6D; green curve). This is mainly attributable to the lower sampling resolution of the Sr-Nd analyse and the fact that the REE-based dust flux represents the total flux. For example, the peak found around 12.0 cal ka BP and 1.7 cal ka BP are not as prominent in the NED flux record because the influence of local volcanic material was removed. As demonstrated by the Sr-Nd isotopes analyses, the dust in Hani peatland is largely derived from the NE drylands (the most likely sources being the Hunshandake and Horqin), so we focus on climatic and environmental records from that region for comparisons. The good agreement between the Hani dust record and the EASM dynamics has been highlighted in previous work (Pratte et al., 2020). A potential influence of the EAWM and WJ on the Hani record was also proposed, but the extent of that influence could not be properly assessed earlier without a more detailed source tracing. Here, the Sr-Nd isotopes analyses allow for a more in depth understanding of the factors influencing the Hani dust record.

The dominance of dust from the NE drylands is generally in accordance with the winter/spring winds from the EAWM. Dust emission from the Gobi desert and the NE drylands is mainly transported by near-surface northwesterly winds to proximal and intermediate regions (Sun et al., 2001). The Hani dust record was compared to EAWM records from north China (Li and Morrill, 2015) and south China (Wang et al., 2012). These two records have good chronostratigraphic constraints, cover most of the period of the Hani record and are strongly correlated to modern EAWM index (Wang et al., 2012) or supported by transient simulations (Li and Morrill, 2015). Peaks in dust deposition in Hani largely occur when EAWM intensity is lower in those records (Fig. 7B and K), especially during the late- and mid-Holocene, suggesting that changes in the deposition rate of dust in Hani are unlikely to be directly or solely related to EAWM intensity. Furthermore, the particle grain size in the Hani record is quite stable, with several peaks coeval with Sr-Nd signatures and Eu/Eu* anomalies (especially around 1.7, 10.7 and 13.0 cal ka BP; Fig. 5 and S1) closer to local volcanic sources. If changes in EAWM-related wind intensity were the main driver of the Hani dust record, greater particle grain sizes would be observed during the late Holocene and between 5.7-3.8 cal ka BP. Changes in the extent of the arid areas or frequency of dust storms in the source region, also potentially related to the EAWM intensity and the Siberian High (Roe, 2009), are more likely explanations for the dust deposition changes in the Hani record. However, the long-term trend in EAWM intensity is opposite to the Hani dust flux, suggesting the EAWM played a limited role at least over the last 10 cal ka BP, a relationship also evidenced in other records (Chen et al., 2021b). There are discrepancies between EAWM records. Some display different patterns with a gradual increase in EAWM strength from the Early to the Late Holocene (Kang et al., 2020; Yang and Ding, 2008), while others display a strong EAWM in the Early and Late Holocene and a weakening in the mid-Holocene (Liu et al., 2020; Yang and Ding, 2014, Xia et al., 2014), a pattern more similar to the Hani dust flux. Discrepancies in reconstructions of EAWM variations are mostly related to chronological uncertainties, proxy sensitivity and sediment resolution. For example, several loess records present hiatus (Kang et al., 2020) or do not possess direct chronologies (Yang and Ding, 2014), especially during the Holocene. Furthermore, loess records on the Chinese Loess Plateau, are not only affected by EAWM changes but also EASM changes (Yang and Ding, 2008), affecting source distance (advance/retreat of desert boundary) (Ding et al., 2005) as well as sediment availability (Stevens et al., 2011), which also influence loess grain size. Diatom-based (south China) and grain size-based (north China) EAWM records

(Li and Morrill, 2015; Wang et al., 2012) indicate a stronger EAWM in the Early Holocene (Fig. 7B), which could partially explain the higher dust flux and proportion from NED during that period. The high dust deposition during the last 2.0 cal ka BP could also be partially explained by an increase in EAWM as suggested by some records (An et al., 2011; Kang et al., 2020). Nevertheless, while the EAWM likely plays a role in dust mobilization and transport, its relationship with the Hani dust record is limited for most of the Holocene.

Changes in the Hani dust record, especially the gradual decrease in dust deposition from the Late Pleistocene to a minimum between 8.0-6.0 cal ka BP (Fig. 6D), are consistent with EASM variability, which controls precipitations (Fig. 6B). In contrast, precipitation records in NE China (Jilin, Liaoning, and Heilongjiang provinces; Fig. 6A) display a distinct pattern than the EASM margin and the Hani dust flux suggesting limited contribution from the region in terms of dust. This contrast in the EASM precipitation between western (EASM margin) and NE China has previously been observed (Zhang et al., 2018b; Zhou et al., 2016). Hence, for clarity we refer to NE China as the region encompassing Liaoning, Jilin and Heilongjiang provinces and the NE drylands (NED) as the drylands along the EASM margin. Moisture and precipitation level are important factors controlling dust emission from drylands by affecting soil moisture and vegetation cover in source regions (Tsoar and Pye, 1987). The evolution (stabilization/reactivation) of the dune fields of the NED (Fig. 6C), located at the margin of the EASM (Fig. 1A), was driven by monsoon precipitations since the Late Glacial (Xu et al., 2020). Dune activity was widespread in the eastern drylands of China during the Late Pleistocene (Yang et al., 2019), the first evidence of dune stabilization being recorded from ~11 cal ka BP. In three drylands of the region (Mu Us, Hunshandake and Horqin; Fig. 1A), the proportion of stabilized dunes increased progressively to reach a maximum around 6.0 cal ka BP (Fig. 6C), the dunes being largely vegetated at that time (Lu et al., 2013). A migration of the monsoon rain belt, up to 400 km to the northwest (Chen et al., 2021a; Goldsmith et al., 2017), along with a ~200 km NW retreat of deserts of northern China (Li et al., 2014) culminating in the mid-Holocene has been proposed. A decrease in monsoonal precipitations and vegetation cover along the EASM margin (Fig. 6B) and related increase dune field activity (Fig. 6C) during the late Holocene are also reflected by an increase in dust deposition in the Hani record (Fig. 6D). The Hani dust record shows an inverse relationship with the general EASM trend along the EASM margin (Fig. 6B and S4), a relationship apparent elsewhere in northern China where a negative correlation of dust with EASM precipitation and vegetation cover was observed (Chen et al., 2021b). During periods of stronger EASM, such as between 6-8 cal ka BP, more precipitation occurs over the NED resulting in a revegetation and stabilization of the dune fields hence generating less dust. This would explain the lower dust deposition rates in Hani peatland during the mid-Holocene. In contrast, the late Holocene drying and southward migration of the EASM and boundary of drylands resulted in a reactivation of the dune fields and in an increase in dust emission reflected by an increase of dust deposition in Hani peatland. This suggests that EASM precipitation and vegetation cover are important control factors of the dust cycle in the region.

4.3 Influence of the WJ on dust variability

The presence of a significant proportion of dust originating from the NMTP deserts (Fig. 3 and 4) in Hani implies an influence of the WJ on dust supply and climate dynamics in the region. The dust flux originating from the NMTP displays an increase after 6 cal ka BP, especially during the late Holocene (Fig. 7K). Changepoint analysis on the NMTP dust flux identified a change significant at >99% at 5.8 cal ka BP. The increase in the NMTP dust flux since 6 cal ka BP also supports a stronger WJ, in line with several WJ records in northern China (Fig. S6A-G). Changes in dust flux have been linked to changes in the strength of the WJ and aridity in the source regions (Ferrat et al., 2012; Lim and Matsumoto, 2008; Sun et al., 2004). Meteorological data have shown that the WJ intensity tends to increase in years of greater dust storm frequency and intensity in Central China (Zhong and Li, 2005). The position of the WJ can also exert an influence on dust deposition in records. The WJ passing over dust source regions for a longer duration of time would result in increased dust uplifting by the WJ, mobilizing more dust, and greater dust deposition downwind (An et al., 2012; Lim and Matsumoto, 2008; Nagashima et al., 2007).

The WJ pathway migrates seasonally through East Asia, being south of the Himalaya (<30°N) in winter and north of the Tibetan Plateau in summer (>42°N) (Schiemann et al., 2009). Recently, evidence points to a control of the seasonal northward position and orientation of the WJ on the EASM rainfall (Chiang et al., 2015; Herzschuh et al., 2019) and by extension on dust (Nagashima et al., 2013). The strength and latitudinal position of the WJ has varied during the Holocene and Late Pleistocene (Herzschuh et al., 2019; Nagashima et al., 2013). Variations in the WJ position were previously reported (Nagashima et al., 2007; Nagashima et al., 2013) using electron spin resonance (ESR) records from sediments from the Sea of Japan (Fig. 7I). Larger ESR values indicate greater inputs from the Mongolian Gobi/NED, reflecting a southward position of the WJ. The WJ was found to be located further south during the Late Pleistocene and between 5.5-3.5 and 1.5-0 cal ka BP affecting the northward extent of the EASM rainbelt (Nagashima et al., 2013). This process could explain the more short-lived peaks in dust flux from NED in Hani, especially between 5.7-3.8 and 1.8-0.3 cal ka BP (Fig. 7K). Several records in the region suggest that the WJ was located further south approximately during the periods of high dust deposition in Hani peatland (Fig. 7G-J). High dust flux periods (Fig. 7J) concurrent with changes in dust composition were found to be related to a southward migration of the summer WJ and changes in land exposure in NW Iran (Sharifi et al., 2015; 2018), while cooling of surface temperatures in the Yellow Sea and mid-latitude Asia were explained a southward migration of the WJ during the same periods (Bae et al., 2020). The relationship between the Hani dust record (Fig. 7K) and EASM rainfall along the EASM margin (Fig. 7C-F) as well as the influence of the WJ, suggest that the Hani dust flux was affected by both the WJ and EASM precipitations. A strengthening or intensification of the WJ is often observed in concurrence with a southward/southeastward shift of its axis (An et al., 2012; Herzschuh et al., 2019). This is confirmed by modelling experiments observing a southward migration and intensification of the summer WJ over Central Asia from 6.5 cal ka BP to the late Holocene with a brief return to a more northward position between 3-2 cal ka BP (Fig 7G; (Zhou et al., 2020). A more southward position of the WJ (Fig. 7G-I) would reduce rainfall at the EASM margin (Fig. 7C-F), resulting in drier conditions in the main dust source region, promoting dust emission from the NE drylands. Several EASM precipitation records near the NE drylands (Fig. 7D-E) display drier conditions suggesting a southeastward retreat of the EASM (Fig. 7F; Wang et al., 2020) between 6.0-4.1 cal ka BP and 2.0-0 cal ka BP when the WJ is further south

and the NED dust deposition in Hani high (Fig. 7K) This interaction between the WJ and EASM would explain the peak in dust observed at 5.8-3.8 and 1.6-0.3 cal ka BP in Hani. Furthermore, with the WJ being further south, the influence of the EAWM is heightened (Nagashima et al., 2007), without having to invoke an intensification, explaining the occurrence of high dust inputs during periods of weaker EAWM. For the Early Holocene and Late Pleistocene, an intensified EAWM (Fig. 7B) combined with a more southward WJ would also have increased the strength of the NW winds resulting in more dust from the NED, but also in greater dust fluxes (Fig. 7K) along with the relatively greater grain size prior to 10 cal ka BP.

The Sr-Nd isotopes record from Hani peatland (Fig. 3 and 5) displays less variability than the ESR records from the Sea of Japan (Fig. 7I) and the isotopic composition of the dust in Neor peatland in Iran (Sharifi et al., 2018). This is likely explainable by the more southerly location of the records from the Sea of Japan (37°04'N) and Iran (37°57'N), making them more sensitive to WJ path changes. Nevertheless, the dust flux record from Hani peatland show striking similarities with the ESR records from the Sea of Japan and the dust flux from Neor peatland in Iran (Fig. 7J). Nagashima et al. (2013) argue that changes in aeolian dust in the Sea of Japan reflect changes in WJ path rather than changes in humidity over the Taklamakan and Mongolian Gobi during the Holocene. While humidity over the Taklamakan and Mongolian Gobi might have not changed significantly, conditions in the northeastern drylands of China, located along the EASM margin and where a large fraction of the dust in Hani peatland is derived from, have changed with a similar timing as the ESR and the Hani dust flux records (Fig. 6 and 7).

Although insolation, through the thermal gradient between high and low latitudes, is the dominant factor explaining changes in the WJ and EASM (Marzin et al., 2013), the spatiotemporal heterogeneity in the Holocene EASM rainfall pattern suggests other paleoclimatic factors also have an effect (Chiang et al., 2015). The timing of the gradual diminution in the dust flux and subsequent mid-Holocene minimum agrees with the overall decrease in ice volume over the early Holocene, reaching a similar extent as today by 7 cal ka BP (Fig. 7A). A notable feature that can be drawn from various paleorecords is that the maximum in EASM (mid-Holocene) in north-central and NE China lags the early-Holocene maximum in insolation (An et al., 2000; Chen et al., 2015). The presence of remnant ice sheets in the Northern Hemisphere (Fig. 7A) is a potential factor for this lag (Marzin et al., 2013) by obstructing the northward migration and deviating the path of the WJ and by extension the EASM front in northern China. Furthermore, the presence of the ice sheet, resulting in lower temperatures in Siberia (Bush, 2005), would have strengthened the Siberian High, possibly contributing to the weakening of the EASM and strengthening of the EAWM during the early Holocene. Other proposed mechanisms include freshwater inputs in the North Atlantic causing a weakening of the AMOC or more frequent El Niño events (especially for the late Holocene), both strengthening the WJ, thereby weakening the EASM (Chen et al., 2015).

Dust is controlled by several factors and its variability is unlikely to be solely attributed to the changes in EASM intensity and the WJ. Some discrepancies between records can be explained by the type of proxy as well as the nature of the records used which each encompass the climatic and dust signal differently. Furthermore, aeolian dust deposition is spatially heterogenous in nature and different factors such as vegetation at the source and deposition site, precipitation amounts at

the study sites, or sedimentation process in the case of lacustrine and marine records will affect the final proxy records and result in potential discrepancies.

In addition to these controlling climatic factors, human activities have increasingly been recognized as a potential contributing factor on the dust cycle in northern China, especially over the last 2 cal ka BP. A dust storm record from lake Gonghai, on the Chinese Loess Plateau, suggests peaks in dust activity occurred during periods of higher monsoonal precipitation and human population, leading the authors to argue for a change from a natural to an anthropogenic forcing on dust over the last 2 cal ka BP in Asia (Chen et al., 2020; Chen et al., 2021b). Lake Gonghai is located in the core area of ancient China with a long history of human occupation, which probably explains the strong influence of human activities on the regional dust cycle. In contrast, human occupation in the region surrounding the main dust source of our study was less prominent and more variable (Guo et al., 2018). Population in Inner Mongolia and Jilin provinces remained near or below 2 million peoples for most of the late Holocene (Fig. 8B). Prior to 0.75 cal ka BP, peak in dust in Hani generally occurred during periods of lower population. Furthermore, for most of the Holocene, period of greater density of archeological sites in NE China (Fig. 8), including the near the drylands, often occur during periods of lower dust deposition in Hani. While a general increasing trend in dust levels over the last 2 cal ka BP is a common feature of several records (He et al., 2015; Wang et al., 2014; Xu et al., 2018), the centennial and decadal variations often display different timing. Discrepancies with several other dust records suggest that the impact of human activities on dust was still very regional in nature. Human activities, mainly millet agriculture, were found to have affected dune dynamics in the Mu Us and Hobq deserts region starting around 2.5 cal ka BP, while the region around the Hunshandake, Horqin and Hulun Buir saw a later development around 1.5 cal ka BP with more intensive activities after 1.0 cal ka BP (Guo et al., 2019; Makohonienko et al., 2004). For example, He et al. (2015) suggest that human impacts on vegetation coverage and dust would have remained secondary to climate factors prior to 250 a cal BP on the NE Tibetan Plateau, as population size and agricultural activities would have been too low in the region. Furthermore, satellite-based measurements of dust optical depth (MODIS) show that 25% of modern global dust emission is of anthropogenic origin (Ginoux et al., 2012). It is expected that late Holocene dust emissions from human activities were lower than modern emissions. While human activities are likely to have increasingly contributed to the dust signal over the late Holocene, especially over the last 1000 years, it is difficult to directly quantify their influence on dust levels and it is premature to ascribe most of dust emissions in the region to human impacts.

4 Conclusions

In this study, we presented a record of the Sr-Nd isotope composition of mineral dust covering the last 14 cal ka BP in a peat sequence from the Changbai Mountains in NE China. The NE drylands (Hunshandake, Horqin) were identified as the main source of the aeolian dust deposited in the record, along with a contribution of the deserts along the northern margin of the Tibetan Plateau (NMTP). The timing of the changes in dust deposition from NED follows the general pattern of EASM precipitations along the EASM margin during the Holocene. The contribution of dust from

the NMTP also suggests an influence of the Westerly Jet on dust and climate dynamics in the region. In summary, we argue that the dust in the Hani peatland likely reflects changes in the surface conditions of the NE drylands (mainly Hunshandake and Horqin) related to variations in EASM rainfall with an influence of the position of the WJ. A stronger and more southerly WJ results in lower monsoonal rainfall over the NE drylands, which in turn increases dust loadings in the region. In the context of the current global warming, changes in the thermal gradient between high and low latitudes would affect the WJ position and strength not only modifying EASM rainfall patterns, but also the dust cycle in the region.

Acknowledgments

The ICP-MS & TIMS services of OMP (A. Lanzanova, C. Duquenoy, S. Mounic) as well as M.-J. Tavella (LEFE) are acknowledged for help with sample preparation and ICP-MS measurements. This research was supported by the Chinese Academy of Sciences President's International Fellowship Initiative (#2017PC0078) to SP, the National Nature Science Foundation of China (NSFC; #41971113) to KB and the NSFC-CNRS Joint Research Project (#41611130163) to KB and FDV. C.L acknowledges financial support from the Swiss National Science Foundation SPF grant TMPFP2_210183.

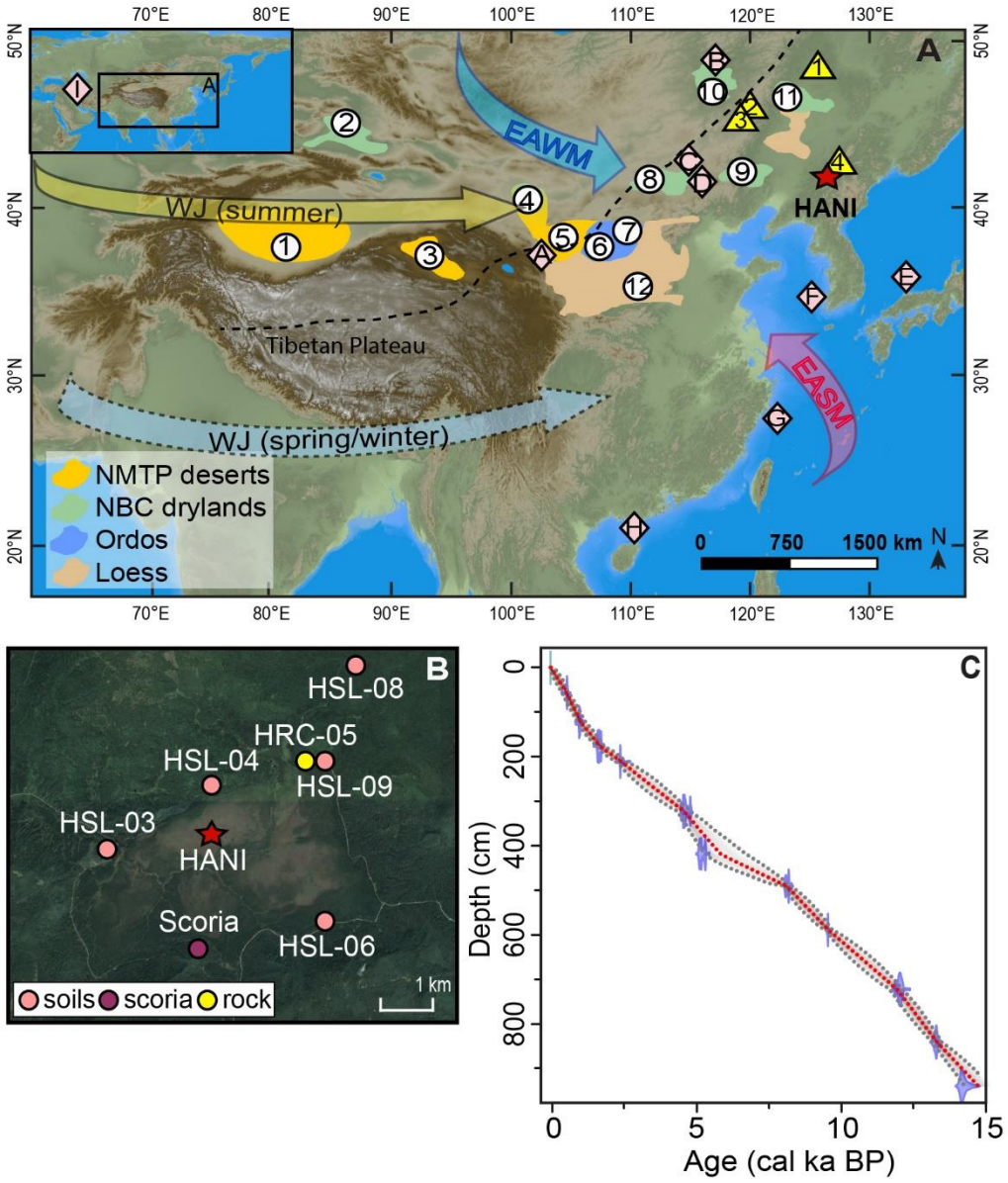

Figure 1. Location of the study region and study site. A) Chinese deserts and drylands (circles). 1. Taklamakan; 2. Gurbantunggut, 3. Qaidam; 4. Badain Jaran; 5. Tengger; 6. Mu Us; 7. Hobq; 8. Hunshandake; 9. Horqin; 10. Hulun Buir; 11. Songnen; 12. Chinese Loess Plateau. Diamonds: relative location of the records discussed in the text: A. Huangyang lake; B. Lake Hulun; C. Lake Bayanchagan; D. Chifeng Loess section, NE China; E. sediment cores D-GC-6 and MD01-2407, Sea of Japan; F. cores HMB-102/HMB-103, SE Yellow Sea; G. core MD06-3040, East China Sea; H. Huguang Maar lake; I. Neor peatland, Iran. Triangles: regional Sr-Nd isotopes records: 1. Lake Tianchi; Lake Tuofengling; 3. Motianling peatland; 4. Lake Sihailongwan. Black dashed line: relative modern limit of the EASM, Chen et al. 2008). NMTP: northern margin of the Tibetan Plateau, NBC: northern boundary of China. Arrows: General trajectories of the main wind systems. B) Location of the Hani-3 core and local sources. C) Age-depth model of the Hani-3 core (details in Pratte et al. (2020)).

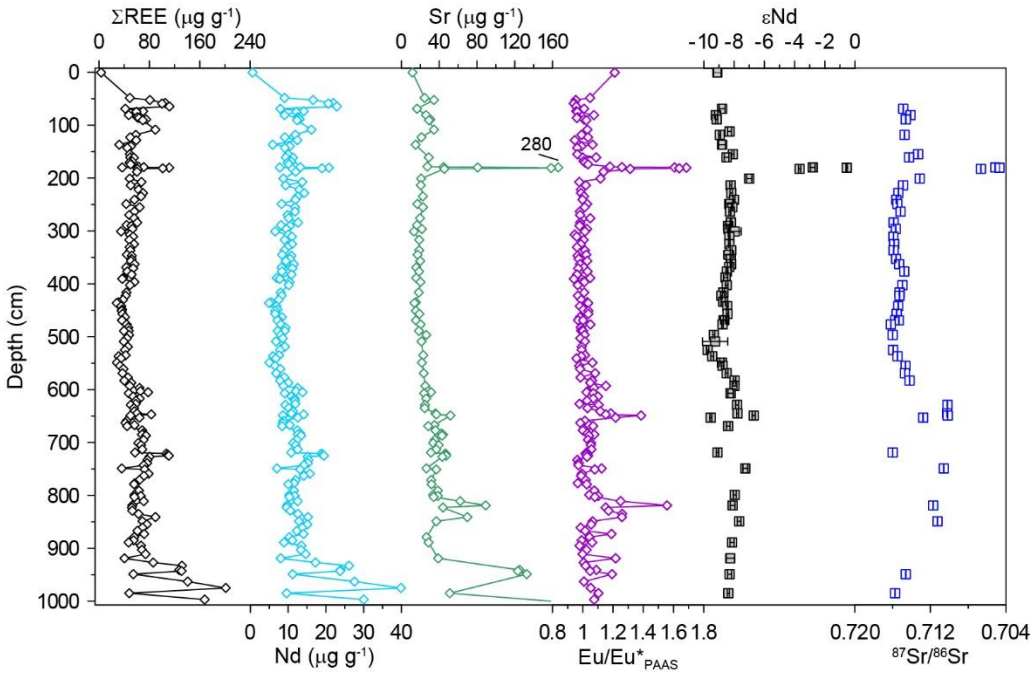

584

585 **Figure 2.** Summary of key data from Hani-3 peat core. Total REE (ΣREE), Nd and Sr
586 concentrations (μg g^{-1}), Eu/Eu^*_{PAAS} (normalized to Post-Archean Australian shale) (Pratte et al.,
587 2020), εNd (this study) and $^{87}Sr/^{86}Sr$ (this study).

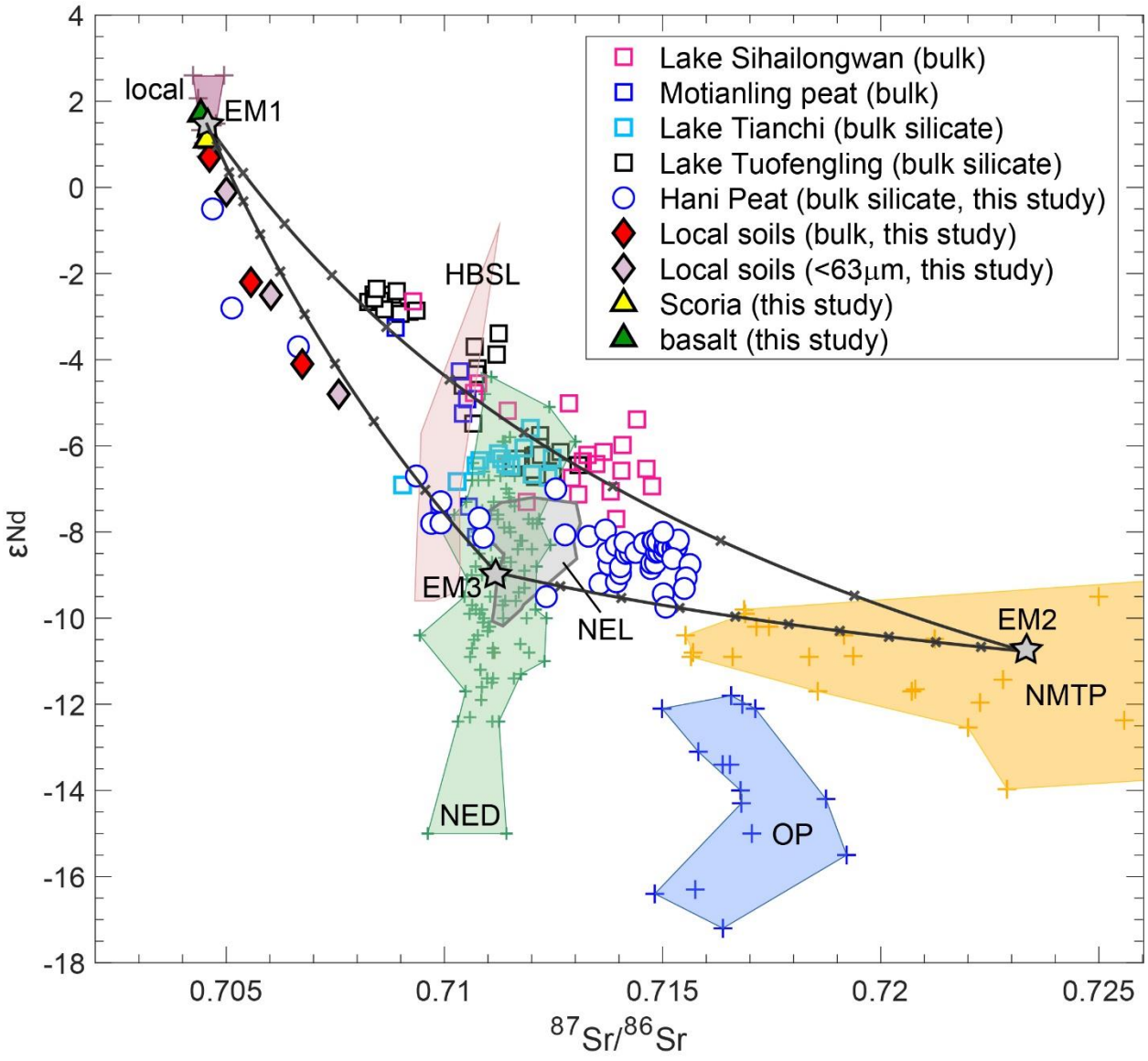

588

589 **Figure 3.** Comparison of εNd vs. $^{87}Sr/^{86}Sr$ of the dust in Hani samples with potential sources.
590 Potential sources of Asian dust: Local (bulk basalts and scoria; Basu et al., 1991; Peng et al., 1986;
591 Yan et al., 2007; Zaarur et al., 2020), NMTP (<75μm; Taklamakan, Qaidam, Tengger; Badain
592 Jaran; (Chen et al., 2007a; Li et al., 2009), Ordos Plateau (OP: <75μm Hobq, Mu Us; Chen et al.,
593 2007a), and NE drylands (NED; Chen et al., 2007a; Xie et al., 2020), Hulun Buir sandy land
594 (HBSL <10μm, <30μm and <63μm; Xie et al., 2017), Gobi (Yang et al., 2009)), NE loess (NEL;
595 <10μm, <30μm and <63μm; Xie et al., 2019; Zeng et al., 2020). Regional records include lake
596 Sihailongwan (Zaarur et al., 2020), lake Tianchi (Zhou et al., 2023), lake Tuofengling (Zhang et
597 al., 2023) and Motianling peatland (Fiałkiewicz-Kozieł et al., 2022). Black lines: end member
598 (stars) mixing lines between local sources (EM1), NMTP (EM2), and NED (EM3), with 10%
599 increments denoted.

600

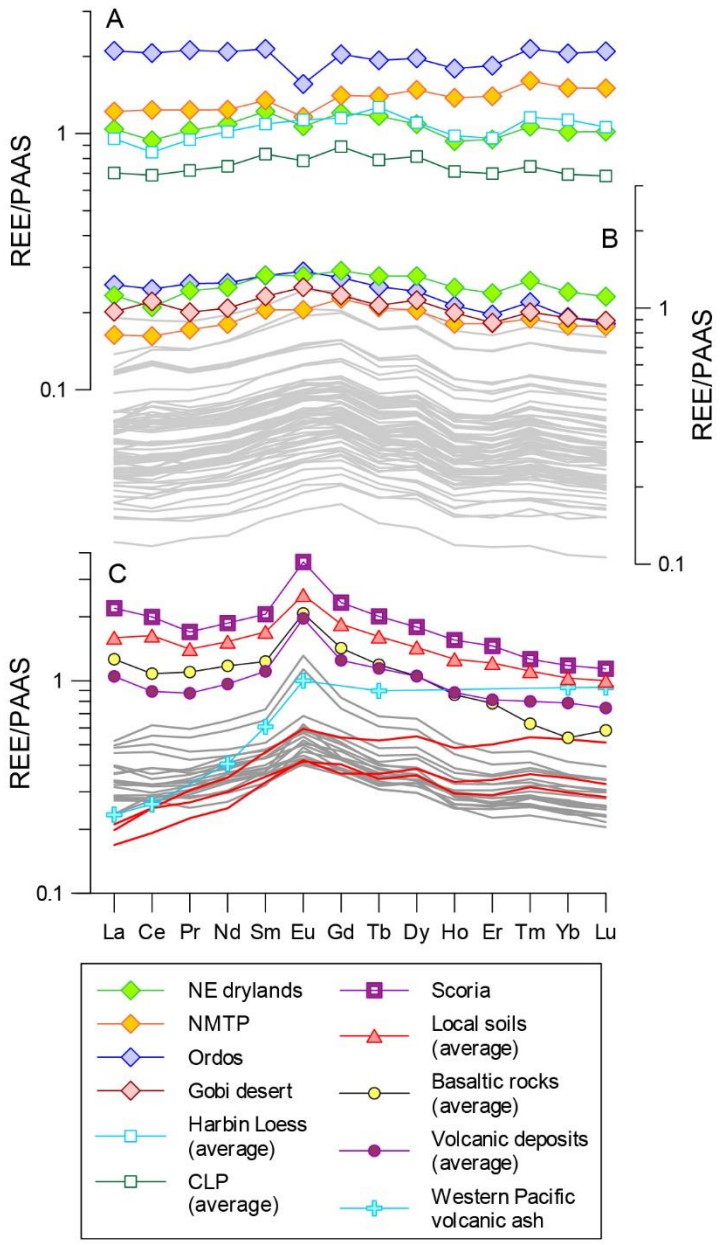

Figure 4. Rare earth element (REE) patterns of Hani peat samples (grey and red curves) normalized to the Post-Archean Australian shales (PAAS; Taylor and McLennan, 1985)). Comparison with average composition of <75 µm (A) and fine <5 µm (B) fractions of deserts/dune fields (diamonds: Ferrat et al., 2011; Hu and Yang, 2016; Jiang and Yang, 2019; Rao et al., 2011; Xie et al., 2019; Xie et al., 2017; Zhang et al., 2018a) and loess (squares: Ferrat et al., 2011; Xie et al., 2017); (C) average composition of local sources: soils, volcanic rocks and volcanic deposits (triangles and dots: this study; Chen et al., 2007b; Liu et al., 2009; Schettler et al., 2006b) and volcanic ash (cross: Bailey, 1993).

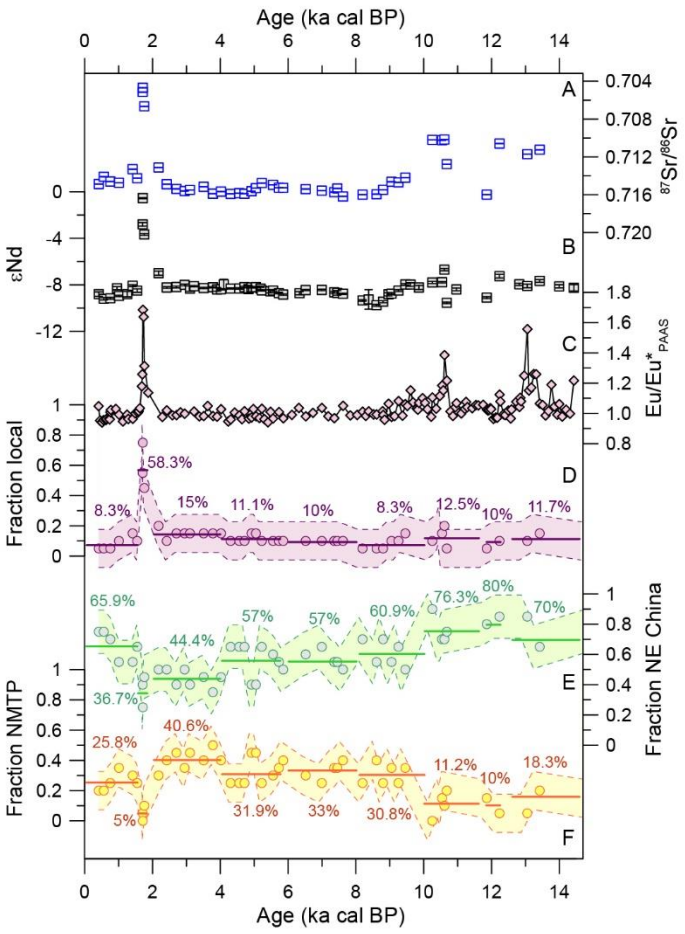

Figure 5. (A) $^{87}Sr/^{86}Sr$, (B) εNd, (C) Eu/Eu*normalized to PAAS (Pratte et al., 2020), and the fraction of dust from end-members EM1 (D), EM2 (E) and EM3 (F). Dashed lines and colored area (D, E, F) represent 1σ uncertainty. Lines in D, E, and F represent average values for each period (1-9) identified in Fig. S1.

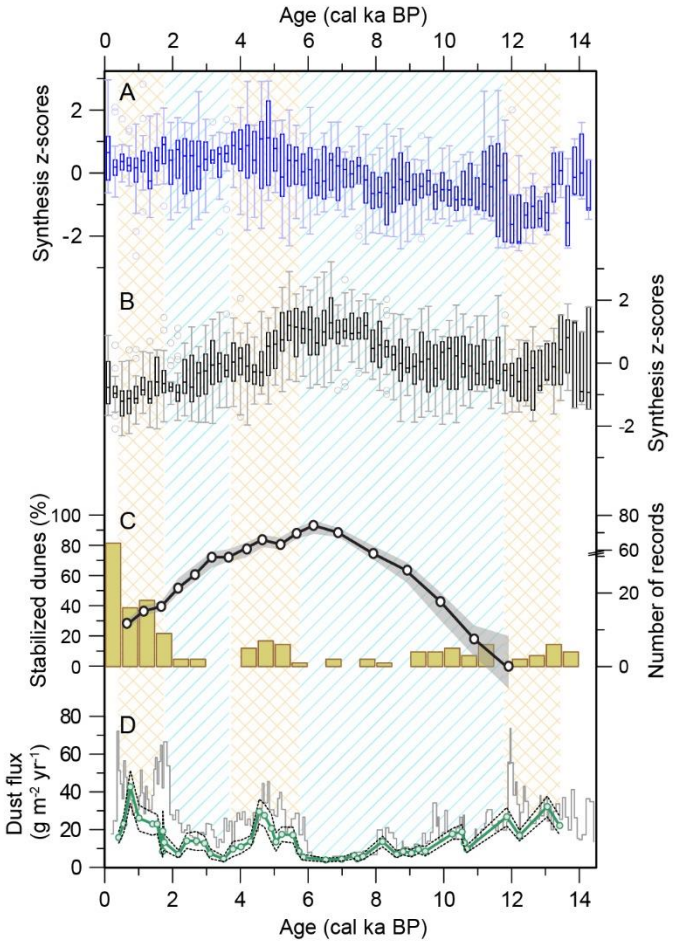

Figure 6. Comparison of the Hani record with records of surface conditions. A) Synthesized humidity/precipitation records for the eastern part of NE China (n=6; from Fig. S5) and B) the EASM margin (n=8; from Fig. S4); C) % of stabilized dunes relative to total in the drylands of northern China (Hunshandake, Horqin, Mu Us; black curve) (Xu et al., 2020) and number of records with mobile dune dates in NE drylands (Hunshandake, Horqin and Hulun Buir; histograms (Guo et al., 2019; Xu et al., 2020); D) REE-based total dust flux (grey step line) and dust flux from NE drylands (green) in Hani-3 core, dashed lines: uncertainties to 1σ. Yellow (higher dust deposition) and blue (lower dust) zones were identified based on change-point analysis.

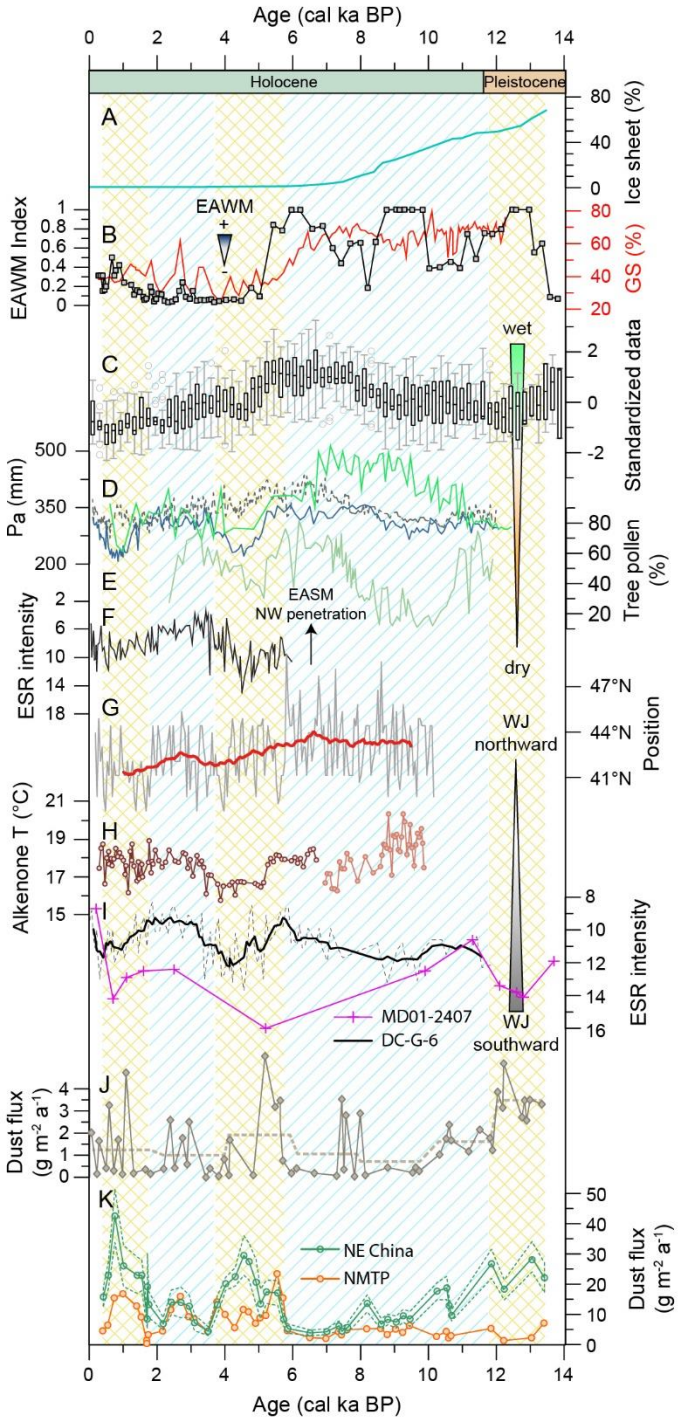

628

629 **Figure 7**. Comparison of the Hani dust record with climatic records. A) % remnant ice sheet in
630 the Northern Hemisphere (Dyke, 2004). B) EAWM intensity indexes: diatom-based index of
631 EAWM intensity from Huguang maar lake (Wang et al., 2012) and grain size-based (GS) index
632 from Huangyang profile (red curve, Li and Morrill, 2015). EASM records: C) Synthesized
633 precipitation record (n=8) from the EASM margin region (from Fig. S4); D) Pollen-based annual
634 precipitation (P_a) reconstruction from Bayanchagan (green), Hulun lake (blue) (Wen et al., 2010)

and Dali lake (dashed line) (Wen et al., 2017); E) Tree pollen % from Diaojiao lake (Shi and Song, 2003); F) Electron spin resonance (ESR) record from core MD06-3040 from the East China Sea (Wang et al., 2020). Indexes of Westerly latitudinal position (selected from Fig. S6): G) simulated latitudinal position of the summer WJ in Central Asia (Zhou et al., 2020); H) Alkenone-based T (°C) record from the Yellow Sea (Bae et al., 2020). I) Electron spin resonance (ESR) intensity in sediment cores from the Japan Sea (Nagashima et al., 2007; Nagashima et al., 2013). J) Ti concentration-based dust flux (solid line) and 2000 years-averaged flux (dashed line) from Neor peatland, Iran (Sharifi et al., 2015); K) Dust flux from NED (green) and NMTP (orange) in Hani-3 core, dashed lines: uncertainties to 1σ. Yellow (higher dust deposition) and blue (lower dust) patterns are the zones determined by change-point analysis on the Hani dust flux.

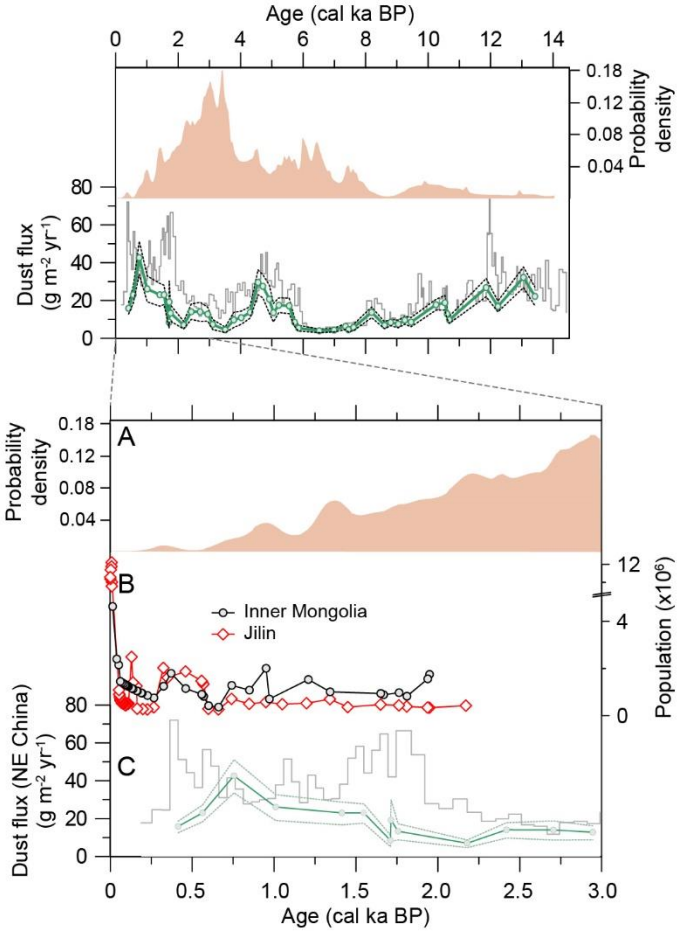

Figure 8. Bottom: Comparison of the Hani dust record with indicators of human activity in the dust source region and NE China. Top: probability density of archeological dates in NE China (including Hunshandake, Horqin) since 14 ka (Wang et al., 2021); Hani REE-based dust flux record. Bottom: A) Probability density of archeological dates in NE China (Wang et al., 2021); B) Historical records of population of the dust source region (Inner Mongolia) and the location of Hani peatland (Jilin) (Zhao and Xie, 1988; Song, 1987a, 1987b); C) Hani REE-based dust flux record.

References

Albarède, F., 1995. Introduction to geochemical modelling. Cambridge University Press, Cambridge.

An, Z., 2000. The history and variability of the East Asian paleomonsoon climate. Quaternary Science Reviews 19, 171-187.

An, Z., Colman, S.M., Zhou, W., Li, X., Brown, E.T., Jull, A.J.T., Cai, Y., Huang, Y., Lu, X., Chang, H., Song, Y., Sun, Y., Xu, H., Liu, W., Jin, Z., Liu, X., Cheng, P., Liu, Y., Ai, L., Li, X., Liu, X., Yan, L., Shi, Z., Wang, X., Wu, F.,

Qiang, X., Dong, J., Lu, F., Xu, X., 2012. Interplay between the Westerlies and Asian monsoon recorded in Lake Qinghai sediments since 32 ka. Scientific Reports 2, 619.
An, Z., Porter, S.C., Kutzbach, J.E., Xihao, W., Suming, W., Xiaodong, L., Xiaoqiang, L., Weijian, Z., 2000. Asynchronous Holocene optimum of the East Asian monsoon. Quaternary Science Reviews 19, 743-762.
Bae, S.W., Lee, K.E., Chang, T.S., 2020. Two long and pronounced cold periods 3,000–5,000 and 6,600–8,400 years B.P. in East Asia and the southward migration of the westerly jet. Palaeogeography, Palaeoclimatology, Palaeoecology 537, 109402.
Bailey, J.C., 1993. Geochemical history of sediments in the northwestern Pacific Ocean. Geochemical Journal 27, 71-90.
Basu, A.R., Wang, J., Huang, W., Xie, G., Tatsumoto, M., 1991. Major element, REE, and Pb, Nd and Sr isotopic geochemistry of Cenozoic volcanic rocks of eastern China: implications for their origin from suboceanic-type mantle reservoirs. Earth Planet Sc Lett 105, 149-169.
Beaudon, E., Sheets, J.M., Martin, E., Sierra-Hernández, M.R., Mosley-Thompson, E., Thompson, L.G., 2022. Aeolian dust preserved in the Guliya ice cap (Northwestern Tibet): a promising paleo-environmental messenger. Geosciences 12, 366.
Biscaye, P.E., Grousset, F.E., Revel, M., Van der Gaast, S., Zielinski, G.A., Vaars, A., Kukla, G., 1997. Asian provenance of glacial dust (stage 2) in the Greenland Ice Sheet Project 2 Ice Core, Summit, Greenland. Journal of Geophysical Research: Oceans 102, 26765-26781.
Bureau of Geology and Mineral Resource of Jilin Province (1988) Regional Geology of Jilin Province. Beijing: Geological Press, pp. 698. (in Chinese).
Bush, A.B.G., 2005. CO2/H2O and orbitally driven climate variability over central Asia through the Holocene. Quaternary International 136, 15-23.
Chen, F., Yu, Z., Yang, M., Ito, E., Wang, S., Madsen, D.B., Huang, X., Zhao, Y., Sato, T., John B. Birks, H., Boomer, I., Chen, J., An, C. and Wünnemann, B. (2008) Holocene moisture evolution in arid central Asia and its out-of-phase relationship with Asian monsoon history. Quaternary Science Reviews 27, 351-364.
Chen, F., Chen, S., Zhang, X., Chen, J., Wang, X., Gowan, E.J., Qiang, M., Dong, G., Wang, Z., Li, Y., Xu, Q., Xu, Y., Smol, J.P., Liu, J., 2020. Asian dust-storm activity dominated by Chinese dynasty changes since 2000 BP. Nature Communications 11, 992.
Chen, F., Xu, Q., Chen, J., Birks, H.J.B., Liu, J., Zhang, S., Jin, L., An, C., Telford, R.J., Cao, X., Wang, Z., Zhang, X., Selvaraj, K., Lu, H., Li, Y., Zheng, Z., Wang, H., Zhou, A., Dong, G., Zhang, J., Huang, X., Bloemendal, J., Rao, Z., 2015. East Asian summer monsoon precipitation variability since the last deglaciation. Scientific Reports 5, 11186.
Chen, J., Li, G., Yang, J., Rao, W., Lu, H., Balsam, W., Sun, Y., Ji, J., 2007a. Nd and Sr isotopic characteristics of Chinese deserts: Implications for the provenances of Asian dust. Geochimica et Cosmochimica Acta 71, 3904-3914.
Chen, J., Zhang, Q., Huang, W., Lu, Z., Zhang, Z., Chen, F., 2021a. Northwestward shift of the northern boundary of the East Asian summer monsoon during the mid-Holocene caused by orbital forcing and vegetation feedbacks. Quaternary Science Reviews 268, 107136.
Chen, S., Liu, J., Wang, X., Zhao, S., Chen, J., Qiang, M., Liu, B., Xu, Q., Xia, D., Chen, F., 2021b. Holocene dust storm variations over northern China: transition from a natural forcing to an anthropogenic forcing. Science Bulletin 66, 2516-2527.
Chen, Y., Zhang, Y., Graham, D., Su, S., Deng, J., 2007b. Geochemistry of Cenozoic basalts and mantle xenoliths in Northeast China. Lithos 96, 108-126.
Chen, Z., Li, G., 2013. Evolving sources of eolian detritus on the Chinese Loess Plateau since early Miocene: Tectonic and climatic controls. Earth Planet Sc Lett 371-372, 220-225.
Chiang, J.C.H., Fung, I.Y., Wu, C.-H., Cai, Y., Edman, J.P., Liu, Y., Day, J.A., Bhattacharya, T., Mondal, Y., Labrousse, C.A., 2015. Role of seasonal transitions and westerly jets in East Asian paleoclimate. Quaternary Science Reviews 108, 111-129.

Chu, G., Sun, Q., Zhaoyan, G., Rioual, P., Qiang, L., Kaijun, W., Han, J., Liu, J., 2009. Dust records from varved lacustrine sediments of two neighboring lakes in northeastern China over the last 1400 years. Quaternary International 194, 108-118.
DePaolo, D.J., Wasserburg, G.J., 1976. Nd isotopic variations and petrogenetic models. Geophysical Research Letters 3, 249-252.
Ding, Z.L., Derbyshire, E., Yang, S.L., Sun, J.M. and Liu, T.S. (2005) Stepwise expansion of desert environment across northern China in the past 3.5 Ma and implications for monsoon evolution. Earth Planet Sc Lett 237, 45-55.
Du, H., Wang, T., Xue, X., Li, S., 2018. Modelling of sand/dust emission in Northern China from 2001 to 2014. Geoderma 330, 162-176.
Dyke, A.S., 2004. An outline of North American deglaciation with emphasis on central and northern Canada, in: Ehlers, J., Gibbard, P.L. (Eds.), Developments in Quaternary Sciences. Elsevier, pp. 373-424.
Feng, J.-L., Zhu, L.-P., Zhen, X.-L., Hu, Z.-G., 2009. Grain size effect on Sr and Nd isotopic compositions in eolian dust: Implications for tracing dust provenance and Nd model age. Geochemical Journal 43, 123-131.
Ferrat, M., Weiss, D.J., Spiro, B., Large, D., 2012. The inorganic geochemistry of a peat deposit on the eastern Qinghai-Tibetan Plateau and insights into changing atmospheric circulation in central Asia during the Holocene. Geochimica et Cosmochimica Acta 91, 7-31.
Ferrat, M., Weiss, D.J., Strekopytov, S., Dong, S., Chen, H., Najorka, J., Sun, Y., Gupta, S., Tada, R., Sinha, R., 2011. Improved provenance tracing of Asian dust sources using rare earth elements and selected trace elements for palaeomonsoon studies on the eastern Tibetan Plateau. Geochimica et Cosmochimica Acta 75, 6374-6399.
Fiałkiewicz-Kozieł, B., Bao, K., Smieja-Król, B., 2022. Geographical drivers of geochemical and mineralogical evolution of Motianling peatland (Northeast China) exposed to different sources of rare earth elements and Pb, Nd, and Sr isotopes. Science of The Total Environment 807, 150481.
Gaiero, D.M., Depetris, P.J., Probst, J.-L., Bidart, S.M., Leleyter, L., 2004. The signature of river- and wind-borne materials exported from Patagonia to the southern latitudes: a view from REEs and implications for paleoclimatic interpretations. Earth Planet Sc Lett 219, 357-376.
Gallet, S., Jahn, B.-m., Van Vliet Lanoë, B., Dia, A., Rossello, E., 1998. Loess geochemistry and its implications for particle origin and composition of the upper continental crust. Earth Planet Sc Lett 156, 157-172.
Ginoux, P., Prospero, J.M., Gill, T.E., Hsu, N.C., Zhao, M., 2012. Global-scale attribution of anthropogenic and natural dust sources and their emission rates based on MODIS Deep Blue aerosol products. Reviews of Geophysics 50.
Ginoux, P., Prospero, J.M., Torres, O., Chin, M., 2004. Long-term simulation of global dust distribution with the GOCART model: correlation with North Atlantic Oscillation. Environmental Modelling & Software 19, 113-128.
Goldsmith, Y., Broecker, W.S., Xu, H., Polissar, P.J., deMenocal, P.B., Porat, N., Lan, J., Cheng, P., Zhou, W., An, Z., 2017. Northward extent of East Asian monsoon covaries with intensity on orbital and millennial timescales. Proceedings of the National Academy of Sciences 114, 1817-1821.
Goudie, A.S., 2009. Dust storms: Recent developments. Journal of Environmental Management 90, 89-94.
Grousset, F.E., Biscaye, P.E., Revel, M., Petit, J.-R., Pye, K., Joussaume, S., Jouzel, J., 1992. Antarctic (Dome C) ice-core dust at 18 k.y. B.P.: Isotopic constraints on origins. Earth Planet Sc Lett 111, 175-182.
Guo, L., Xiong, S., Dong, X., Ding, Z., Yang, P., Zhao, H., Wu, J., Ye, W., Jin, G., Wu, W., Zheng, L., 2019. Linkage between C4 vegetation expansion and dune stabilization in the deserts of NE China during the late Quaternary. Quaternary International 503, 10-23.
He, Y., Zhao, C., Song, M., Liu, W., Chen, F., Zhang, D., Liu, Z., 2015. Onset of frequent dust storms in northern China at ~AD 1100. Scientific Reports 5, 17111.

763 Herzschuh, U., Cao, X., Laepple, T., Dallmeyer, A., Telford, R.J., Ni, J., Chen, F., Kong, Z., Liu, G., Liu, K.-B.,
764 Liu, X., Stebich, M., Tang, L., Tian, F., Wang, Y., Wischnewski, J., Xu, Q., Yan, S., Yang, Z., Yu, G., Zhang, Y.,
765 Zhao, Y., Zheng, Z., 2019. Position and orientation of the westerly jet determined Holocene rainfall
766 patterns in China. Nature Communications 10, 2376.
767 Hu, F., Yang, X., 2016. Geochemical and geomorphological evidence for the provenance of aeolian
768 deposits in the Badain Jaran Desert, northwestern China. Quaternary Science Reviews 131, 179-192.
769 Jacobsen, S.B., Wasserburg, G.J., 1980. Sm-Nd isotopic evolution of chondrites. Earth Planet Sc Lett 50,
770 139-155.
771 Jiang, Q., Yang, X., 2019. Sedimentological and Geochemical Composition of Aeolian Sediments in the
772 Taklamakan Desert: Implications for Provenance and Sediment Supply Mechanisms. Journal of
773 Geophysical Research: Earth Surface 124, 1217-1237.
774 Kohfeld, K.E., Harrison, S.P., 2001. DIRTMAP: the geological record of dust. Earth-Science Reviews 54, 81-
775 114.
776 Kang, S., Du, J., Wang, N., Dong, J., Wang, D., Wang, X., Qiang, X. and Song, Y. (2020) Early Holocene
777 weakening and mid- to late Holocene strengthening of the East Asian winter monsoon. Geology 48, 1043-
778 1047.
779 Le Roux, G., Fagel, N., De Vleeschouwer, F., Krachler, M., Debaille, V., Stille, P., Mattielli, N., van der Knaap,
780 W.O., van Leeuwen, J.F.N., Shotyk, W., 2012. Volcano- and climate-driven changes in atmospheric dust
781 sources and fluxes since the Late Glacial in Central Europe. Geology 40, 335-338.
782 Letelier, R.M., Björkman, K.M., Church, M.J., Hamilton, D.S., Mahowald, N.M., Scanza, R.A., Schneider, N.,
783 White, A.E., Karl, D.M., 2019. Climate-driven oscillation of phosphorus and iron limitation in the North
784 Pacific Subtropical Gyre. Proceedings of the National Academy of Sciences 116, 12720-12728.
785 Li, C., Sonke, J.E., Le Roux, G., Van der Putten, N., Piotrowska, N., Jeandel, C., Mattielli, N., Benoit, M.,
786 Wiggs, G.F.S., De Vleeschouwer, F., 2020. Holocene dynamics of the southern westerly winds over the
787 Indian Ocean inferred from a peat dust deposition record. Quaternary Science Reviews 231, 106169.
788 Li, G., Chen, J., Ji, J., Yang, J., Conway, T.M., 2009. Natural and anthropogenic sources of East Asian dust.
789 Geology 37, 727-730.
790 Li, G., Wang, Z., Zhao, W., Jin, M., Wang, X., Tao, S., Chen, C., Cao, X., Zhang, Y., Yang, H. and Madsen, D.
791 (2020a) Quantitative precipitation reconstructions from Chagan Nur revealed lag response of East Asian
792 summer monsoon precipitation to summer insolation during the Holocene in arid northern China.
793 Quaternary Science Reviews 239, 106365.
794 Li, G., Zhang, H., Liu, X., Yang, H., Wang, X., Zhang, X., Jonell, T.N., Zhang, Y., Huang, X., Wang, Z., Yixuan,
795 W., Yu, L. and Xia, D. (2020b) Paleoclimatic changes and modulation of East Asian summer monsoon by
796 high-latitude forcing over the last 130,000 years as revealed by independently dated loess-paleosol
797 sequences on the NE Tibetan Plateau. Quaternary Science Reviews 237, 106283.
798 Li, Q., Wu, H., Guo, Z., Yu, Y., Ge, J., Wu, J., Zhao, D., Sun, A., 2014. Distribution and vegetation
799 reconstruction of the deserts of northern China during the mid-Holocene. Geophysical Research Letters
800 41, 5184-5191.
801 Li, Y., Morrill, C., 2015. A Holocene East Asian winter monsoon record at the southern edge of the Gobi
802 Desert and its comparison with a transient simulation. Climate Dynamics 45, 1219-1234.
803 Liu, J., Chu, G., Han, J., Rioual, P., Jiao, W., Wang, K., 2009. Volcanic eruptions in the Longgang volcanic
804 field, northeastern China, during the past 15,000 years. Journal of Asian Earth Sciences 34, 645-654.
805 Liu, X., Sun, Y., Vandenberghe, J., Cheng, P., Zhang, X., Gowan, E.J., Lohmann, G. and An, Z. (2020)
806 Centennial- to millennial-scale monsoon changes since the last deglaciation linked to solar activities and
807 North Atlantic cooling. Clim. Past 16, 315-324.
808 Lu, H., Yi, S., Xu, Z., Zhou, Y., Zeng, L., Zhu, F., Feng, H., Dong, L., Zhuo, H., Yu, K., Mason, J., Wang, X., Chen,
809 Y., Lu, Q., Wu, B., Dong, Z., Qu, J., Wang, X., Guo, Z., 2013. Chinese deserts and sand fields in Last Glacial
810 Maximum and Holocene Optimum. Chinese Science Bulletin 58, 2775-2783.

Makohonienko, M., Kitagawa, H., Naruse, T., Nasu, H., Momohara, A., Okuno, M., Fujiki, T., Liu, X., Yasuda, Y., Yi, H., 2004. Late-Holocene natural and anthropogenic vegetation changes in the Dongbei Pingyuan (Manchurian Plain), northeastern China. Quaternary International 123-125, 71-88.
Makohonienko, M., Kitagawa, H., Fujiki, T., Liu, X., Yasuda, Y., Yin, H., 2008. Late Holocene vegetation changes and human impact in the Changbai Mountains area, Northeast China. Quaternary International 184, 94-108.
Marx, S.K., Kamber, B.S., McGowan, H.A., Petherick, L.M., McTainsh, G.H., Stromsoe, N., Hooper, J.N., May, J.-H., 2018. Palaeo-dust records: A window to understanding past environments. Global and Planetary Change 165, 13-43.
Marzin, C., Braconnot, P., Kageyama, M., 2013. Relative impacts of insolation changes, meltwater fluxes and ice sheets on African and Asian monsoons during the Holocene. Climate Dynamics 41, 2267-2286.
McLennan, S.M., 1989. Rare earth elements in sedimentary rocks; influence of provenance and sedimentary processes. Reviews in Mineralogy and Geochemistry 21, 169-200.
Meyer, I., Davies, G.R., Stuut, J.-B.W., 2011. Grain size control on Sr-Nd isotope provenance studies and impact on paleoclimate reconstructions: An example from deep-sea sediments offshore NW Africa. Geochemistry, Geophysics, Geosystems 12.
Miyazaki, T., Kimura, J.-I., Katakuse, M., 2016. Geochemical records from loess deposits in Japan over the last 210 kyr: Lithogenic source changes and paleoclimatic indications. Geochemistry, Geophysics, Geosystems 17, 2745-2761.
Nagashima, K., Tada, R., Tani, A., Toyoda, S., Sun, Y., Isozaki, Y., 2007. Contribution of aeolian dust in Japan Sea sediments estimated from ESR signal intensity and crystallinity of quartz. Geochemistry, Geophysics, Geosystems 8.
Nagashima, K., Tada, R., Toyoda, S., 2013. Westerly jet-East Asian summer monsoon connection during the Holocene. Geochemistry, Geophysics, Geosystems 14, 5041-5053.
Nakano, T., Yokoo, Y., Nishikawa, M., Koyanagi, H., 2004. Regional Sr–Nd isotopic ratios of soil minerals in northern China as Asian dust fingerprints. Atmospheric Environment 38, 3061-3067.
Nesbitt, H.W., 1979. Mobility and fractionation of rare earth elements during weathering of a granodiorite. Nature 279, 206.
Peng, Z.C., Zartman, R.E., Futa, K., Chen, D.G., 1986. Pb-, Sr- and Nd-isotopic systematics and chemical characteristics of Cenozoic basalts, eastern China. Chemical Geology: Isotope Geoscience section 59, 3-33.
Pratte, S., Bao, K., Sapkota, A., Zhang, W., Shen, J., Le Roux, G., De Vleeschouwer, F., 2020. 14 kyr of atmospheric mineral dust deposition in north-eastern China: A record of palaeoclimatic and palaeoenvironmental changes in the Chinese dust source regions. The Holocene 30, 492-506.
Pratte, S., Garneau, M., De Vleeschouwer, F., 2017. Late-Holocene atmospheric dust deposition in eastern Canada (St. Lawrence North Shore). The Holocene 27, 12-25.
Rao, W., Chen, J.U.N., Yang, J., Ji, J., Li, G., Tan, H., 2008. Sr-Nd isotopic characteristics of eolian deposits in the Erdos Desert and Chinese Loess Plateau: Implications for their provenances. Geochemical Journal 42, 273-282.
Rao, W., Tan, H., Jiang, S., Chen, J., 2011. Trace element and REE geochemistry of fine- and coarse-grained sands in the Ordos deserts and links with sediments in surrounding areas. Geochemistry 71, 155-170.
Roe, G., 2009. On the interpretation of Chinese loess as a paleoclimate indicator. Quaternary Research 71, 150-161.
Schettler, G., Liu, Q., Mingram, J., Negendank, J.F.W., 2006a. Palaeovariations in the East-Asian Monsoon Regime Geochemically Recorded in Varved Sediments of Lake Sihailongwan (Northeast China, Jilin Province). Part 1: Hydrological Conditions and Dust Flux. Journal of Paleolimnology 35, 239-270.
Schettler, G., Mingram, J., Negendank, J.F.W., Jiaqi, L., 2006b. Palaeovariations in the East-Asian Monsoon Regime Geochemically Recorded in Varved Sediments of Lake Sihailongwan (Northeast China, Jilin

Province). Part 2: a 200-Year Record of Atmospheric Lead-210 Flux Variations and its Palaeoclimatic Implications. Journal of Paleolimnology 35, 271-288.
Schiemann, R., Lüthi, D., Schär, C., 2009. Seasonality and Interannual Variability of the Westerly Jet in the Tibetan Plateau Region. Journal of Climate 22, 2940-2957.
Sharifi, A., Murphy, L.N., Pourmand, A., Clement, A.C., Canuel, E.A., Naderi Beni, A., A.K. Lahijani, H., Delanghe, D., Ahmady-Birgani, H., 2018. Early-Holocene greening of the Afro-Asian dust belt changed sources of mineral dust in West Asia. Earth Planet Sc Lett 481, 30-40.
Sharifi, A., Pourmand, A., Canuel, E.A., Ferer-Tyler, E., Peterson, L.C., Aichner, B., Feakins, S.J., Daryaee, T., Djamali, M., Beni, A.N., Lahijani, H.A.K., Swart, P.K., 2015. Abrupt climate variability since the last deglaciation based on a high-resolution, multi-proxy peat record from NW Iran: The hand that rocked the Cradle of Civilization? Quaternary Science Reviews 123, 215-230.
Shi, P., Song, C., 2003. Palynological records of environmental changes in the middle part of Inner Mongolia, China. Chinese Science Bulletin 48, 1433-1438.
Shotyk, W., 1997. Atmospheric deposition and mass balance of major and trace elements in two oceanic peat profiles, northern Scotland and Shetland Islands. Chemical Geology 138, 55-72.
Song, Q., 1987a. Chinese Population: Inner Mongolia Branch. China Financial and Economic Publishing House. (in Chinese)
Song, Q., 1987b. Chinese Population: Jilin Branch. China Financial and Economic Publishing House. (in Chinese)
Steinmann, P., Shotyk, W., 1997. Geochemistry, mineralogy, and geochemical mass balance on major elements in two peat bog profiles (Jura Mountains, Switzerland). Chemical Geology 138, 25-53.
Stevens, T., Marković, S.B., Zech, M., Hambach, U. and Sümegi, P. (2011) Dust deposition and climate in the Carpathian Basin over an independently dated last glacial–interglacial cycle. Quaternary Science Reviews 30, 662-681.
Sun, D., Bloemendal, J., Rea, D.K., An, Z., Vandenberghe, J., Lu, H., Su, R. and Liu, T. (2004) Bimodal grain-size distribution of Chinese loess, and its palaeoclimatic implications. CATENA 55, 325-340.
Sun, J., Zhang, M., Liu, T., 2001. Spatial and temporal characteristics of dust storms in China and its surrounding regions, 1960–1999: Relations to source area and climate. Journal of Geophysical Research: Atmospheres 106, 10325-10333.
Taylor, S.R., McLennan, S.M., 1985. The continental crust: Its composition and evolution. Blackwell Scientific, Oxford.
Taylor, W., 2000. Change-point analysis: A powerful new tool for detecting changes. Retrieved from: http://www.variation.com/cpa/techchangepoint.html
Tsoar, H., Pye, K., 1987. Dust transport and the question of desert loess formation. Sedimentology 34, 139-153.
Vanneste, H., De Vleeschouwer, F., Martínez-Cortizas, A., von Scheffer, C., Piotrowska, N., Coronato, A., Le Roux, G., 2015. Late-glacial elevated dust deposition linked to westerly wind shifts in southern South America. Scientific Reports 5.
Wang, H., Chen, J., Zhang, X., Chen, F., 2014. Palaeosol development in the Chinese Loess Plateau as an indicator of the strength of the East Asian summer monsoon: Evidence for a mid-Holocene maximum. Quaternary International 334-335, 155-164.
Wang, K., Tada, R., Zheng, H., Irino, T., Zhou, B., Saito, K., 2020. Provenance changes in fine detrital quartz in the inner shelf sediments of the East China Sea associated with shifts in the East Asian summer monsoon front during the last 6 kyrs. Progress in Earth and Planetary Science 7, 5.
Wang, L., Li, J., Lu, H., Gu, Z., Rioual, P., Hao, Q., Mackay, A.W., Jiang, W., Cai, B., Xu, B., Han, J., Chu, G., 2012. The East Asian winter monsoon over the last 15,000 years: its links to high-latitudes and tropical climate systems and complex correlation to the summer monsoon. Quaternary Science Reviews 32, 131-142.

Wedepohl, K.H., 1995. The composition of the continental crust. Geochimica et Cosmochimica Acta 59, 1217-1232.
Wen, R., Xiao, J., Chang, Z., Zhai, D., Xu, Q., Li, Y., Itoh, S., 2010. Holocene precipitation and temperature variations in the East Asian monsoonal margin from pollen data from Hulun Lake in northeastern Inner Mongolia, China. Boreas 39, 262-272.
Wen, R., Xiao, J., Fan, J., Zhang, S., Yamagata, H., 2017. Pollen evidence for a mid-Holocene East Asian summer monsoon maximum in northern China. Quaternary Science Reviews 176, 29-35.
Wilson, M., 2000. Igneous Petrogenesis: A Global Tectonic Approach. Kluwer Academic Publishers, London
Xia, D., Jia, J., Li, G., Zhao, S., Wei, H. and Chen, F. (2014) Out-of-phase evolution between summer and winter East Asian monsoons during the Holocene as recorded by Chinese loess deposits. Quaternary Research 81, 500-507.
Xie, Y., Chi, Y., 2016. Geochemical investigation of dry- and wet-deposited dust during the same dust-storm event in Harbin, China: Constraint on provenance and implications for formation of aeolian loess. Journal of Asian Earth Sciences 120, 43-61.
Xie, Y., Kang, C., Chi, Y., Du, H., Wang, J., Sun, L., 2019. The loess deposits in Northeast China: The linkage of loess accumulation and geomorphic-climatic features at the easternmost edge of the Eurasian loess belt. Journal of Asian Earth Sciences 181, 103914.
Xie, Y., Liu, L., Kang, C., Chi, Y., 2020. Sr-Nd isotopic characteristics of the Northeast Sandy Land, China and their implications for tracing sources of regional dust. Catena 184, 104303.
Xie, Y., Yuan, F., Zhan, T., Kang, C., Chi, Y., Ma, Y., 2017. Geochemistry of loess deposits in northeastern China: constraint on provenance and implication for disappearance of the large Songliao palaeolake. Journal of the Geological Society 175, 146-162.
Xu, B., Wang, L., Gu, Z., Hao, Q., Wang, H., Chu, G., Jiang, D., Liu, Q., Qin, X., 2018. Decoupling of Climatic Drying and Asian Dust Export During the Holocene. Journal of Geophysical Research: Atmospheres 123, 915-928.
Xu, Z., Mason, J.A., Xu, C., Yi, S., Bathiany, S., Yizhaq, H., Zhou, Y., Cheng, J., Holmgren, M., Lu, H., 2020. Critical transitions in Chinese dunes during the past 12,000 years. Science Advances 6, eaay8020.
Yan, J., Zhao , J.X., Liu, H.Q., 2007. Quaternary basalts from Longgang in the North China Craton: petrologenesis and characteristics of the mantle source. Acta Petrologica Sinica 23, 1413-1422. (in Chinese)
Yang, J., Li, G., Rao, W., Ji, J., 2009. Isotopic evidences for provenance of East Asian Dust. Atmospheric Environment 43, 4481-4490.
Yang, S. and Ding, Z. (2008) Advance–retreat history of the East-Asian summer monsoon rainfall belt over northern China during the last two glacial–interglacial cycles. Earth Planet Sc Lett 274, 499-510.
Yang, S. and Ding, Z. (2014) A 249 kyr stack of eight loess grain size records from northern China documenting millennial-scale climate variability. Geochemistry, Geophysics, Geosystems 15, 798-814.
Yang, X., Liang, P., Zhang, D., Li, H., Rioual, P., Wang, X., Xu, B., Ma, Z., Liu, Q., Ren, X., Hu, F., He, Y., Rao, G., Chen, N., 2019. Holocene aeolian stratigraphic sequences in the eastern portion of the desert belt (sand seas and sandy lands) in northern China and their palaeoenvironmental implications. Science China Earth Sciences 62, 1302-1315.
Zaarur, S., Stein, M., Adam, O., Mingram, J., Liu, J., Wu, J., Raveh-Rubin, S., Erel, Y., 2020. Synoptic stability and anomalies in NE China inferred from dust provenance of Sihailongwan maar sediments during the past ~80 kyr. Quaternary Science Reviews 239, 106279.
Zeng, L., Yi, S., Zhang, W., Feng, H., Lv, A., Zhao, W., Luo, Y., Wang, Q., Lu, H., 2020. Provenance of loess deposits and stepwise expansion of the desert environment in NE China since ~1.2 Ma: Evidence from Nd-Sr isotopic composition and grain-size record. Global and Planetary Change 185, 103087.
Zhang, K., Gao, H., 2007. The characteristics of Asian-dust storms during 2000–2002: From the source to the sea. Atmospheric Environment 41, 9136-9145.

Zhang, M., Bu, Z., Jiang, M., Wang, S., Liu, S., Chen, X., Hao, J., Liao, W., 2019. The development of Hani peatland in the Changbai mountains (NE China) and its response to the variations of the East Asian summer monsoon. Science of The Total Environment 692, 818-832.
Zhang, W., Chen, J., Ji, J., Li, G., 2016. Evolving flux of Asian dust in the North Pacific Ocean since the late Oligocene. Aeolian Research 23, 11-20.
Zhang, W., Hou, S., Liu, Y., Wu, S., An, W., Pang, H., Wang, C., 2017. A high-resolution atmospheric dust record for 1810–2004 A.D. derived from an ice core in eastern Tien Shan, central Asia. Journal of Geophysical Research: Atmospheres 122, 7505-7518.
Zhang, W., Zhang, E., Liu, E., Abell, J.T., Sun, W., Ni, Z., Chen, R., Cai, Y., Meng, X., 2023. Mongolian dust activity over the last 25 kyr predominantly driven by the East Asian winter monsoon: insights from the geochemistry of lake Tuofengling sediments. Geophysical Research Letters 50, e2023GL103633.
Zhang, W., Zhao, J.-x., Chen, J., Ji, J., Liu, L., 2018a. Binary sources of Chinese loess as revealed by trace and REE element ratios. Journal of Asian Earth Sciences 166, 80-88.
Zhang, X., Jin, L., Lu, H., Park, W., Schneider, B., Latif, M., 2018b. East–west contrast of Northeast Asian summer precipitation during the Holocene. Global and Planetary Change 170, 190-200.
Zhao, H., Liu, J., Hall, V.A., Li, X., 2017. Tephrostratigraphical investigation of lake sediments and a peat bog in Northeastern China since 20,000 years. The Holocene 27, 765-778.
Zhao, W., Sun, Y., Balsam, W., Zeng, L., Lu, H., Otgonbayar, K., Ji, J., 2015. Clay-sized Hf-Nd-Sr isotopic composition of Mongolian dust as a fingerprint for regional to hemispherical transport. Geophysical Research Letters 42, 5661-5669.
Zhao, W., Xie, S., 1988. Human population in China. People's Publishing House, Beijing. (in Chinese)
Zhong, H., Li, D., 2005. Relationship between sand dust storm in northern China in April and Westerly Circulation. Plateau Meteorology 24, 104–111. (in Chinese)
Zhou, P., Shi, Z., Li, X., Zhou, W., 2020. Response of Westerly Jet over the Northern Hemisphere to astronomical insolation during the Holocene. Frontiers in Earth Science 8.
Zhou, X., Sun, L., Zhan, T., Huang, W., Zhou, X., Hao, Q., Wang, Y., He, X., Zhao, C., Zhang, J., Qiao, Y., Ge, J., Yan, P., Yan, Q., Shao, D., Chu, Z., Yang, W., Smol, J.P., 2016. Time-transgressive onset of the Holocene Optimum in the East Asian monsoon region. Earth Planet Sc Lett 456, 39-46.
Zhou, X., Zhan, T., Tan, N., Tu, L., Smol, J.P., Jiang, S., Zeng, F., Liu, X., Li, X., Liu, G., Liu, Y., Zhang, R., Shen, Y., 2023. Inconsistent patterns of Holocene rainfall changes at the East Asian monsoon margin compared to the core monsoon region. Quaternary Science Reviews 301, 107952.